

# Closed-loop control of unsteadiness over a rounded backward-facing step

Alexandre Barbagallo<sup>1,2</sup>, Gregory Dergham<sup>3</sup>, Denis Sipp<sup>1</sup>, Peter J. Schmid<sup>2†</sup>  
and Jean-Christophe Robinet<sup>3</sup>

<sup>1</sup> ONERA – The French Aerospace Lab, 8 rue des Vertugadins, 92190 Meudon, France

<sup>2</sup> Laboratoire d’Hydrodynamique (LadHyX), CNRS – Ecole Polytechnique, 91128 Palaiseau, France

<sup>3</sup> DynFluid Laboratory, Arts et Metiers ParisTech, 151 Boulevard de l’Hôpital, 75013 Paris, France

(Received 22 October 2010; revised 8 March 2012; accepted 8 May 2012;  
first published online 12 June 2012)

The two-dimensional, incompressible flow over a rounded backward-facing step at Reynolds number  $Re = 600$  is characterized by a detachment of the flow close to the step followed by a recirculation zone. Even though the flow is globally stable, perturbations are amplified as they are convected along the shear layer, and the presence of upstream random noise renders the flow unsteady, leading to a broadband spectrum of excited frequencies. This paper is aimed at suppressing this unsteadiness using a controller that converts a shear-stress measurement taken from a wall-mounted sensor into a control law that is supplied to an actuator. A comprehensive study of various components of closed-loop control design – covering sensor placement, choice and influence of the cost functional, accuracy of the reduced-order model, compensator stability and performance – shows that successful control of this flow requires a judicious balance between estimation speed and estimation accuracy, and between stability limits and performance requirements. The inherent amplification behaviour of the flow can be reduced by an order of magnitude if the above-mentioned constraints are observed. In particular, to achieve superior controller performance, the estimation sensor should be placed upstream near the actuator to ensure sufficient estimation speed. Also, if high-performance compensators are sought, a very accurate reduced-order model is required, especially for the dynamics between the actuator and the estimation sensor; otherwise, very minute errors even at low energies and high frequencies may render the large-scale compensated linearized simulation unstable. Finally, coupling the linear compensator to nonlinear simulations shows a gradual deterioration in control performance as the amplitude of the noise increases.

**Key words:** boundary layer control, control theory, separated flows

---

## 1. Introduction

Many industrial fluid devices are afflicted by undesirable flow behaviour – such as unsteadiness, separation, instabilities and transition to turbulence – which limits performance, endangers safe operation or is detrimental to structural components. Flow control is quickly becoming a key technology in engineering design to overcome

† Email address for correspondence: [peter@ladhyx.polytechnique.fr](mailto:peter@ladhyx.polytechnique.fr)

inherent limitations, to advance into unexplored parameter regimes, to extend safety margins and to ensure operation under optimal conditions. A prototypical and much-studied example is the compressible flow over a cavity, which is characterized by instabilities that manifest themselves in a buffeting motion, in induced drag (Gharib & Roshko 1987) and in intense noise emission (see Rossiter 1964). In the air intakes of aircraft engines, separated flow can act as an amplifier for incoming perturbations, causing unsteadiness, which in turn results in loss of performance and material fatigue. Transitional and turbulent boundary layers have long attracted the attention of the flow control community (see e.g. Joslin 1998; Kim 2003; Saric, Reed & White 2003; Archambaud *et al.* 2008; Boiko, Dovgal & Hein 2008), mainly as a result of their ubiquity in vehicle aerodynamics and their central role as the source of skin friction. For all three examples, flow control techniques that effectively eliminate instabilities, efficiently reduce noise amplification or successfully diminish drag are essential in maintaining the desired flow conditions.

The design procedure of flow control laws critically depends on the nature of the flow to be controlled. Oscillator-type flows, which are defined by a global instability resulting in self-sustained oscillatory fluid behaviour, are more easily controlled, since the flow is dominated by a limited number of structures of well-defined frequencies. Sensitivity to noise is comparatively low, and the estimator and controller can simply reconstruct the flow state from measurements and act upon it according to the control objective. A second type of flow behaviour, referred to as noise amplifiers, is substantially more challenging to control. This type of flow is globally stable but is characterized by a strong propensity to amplify noise and a broadband spectrum of responsive frequencies. These characteristics make the flow and the control performance highly sensitive, not only to physical noise sources and uncertainties, but also to the methodological approximations, modelling inaccuracies and truncation errors that inevitably arise during estimator and control design. The propagation of small perturbations, whether of physical or computational origin, is appropriately tracked and quantified by frequency-based transfer functions, which reveal preferred frequencies or confirm the successful reduction of the flow's amplification potential.

Optimal flow control techniques have been widely applied for active control purposes. In particular, the linear quadratic Gaussian (LQG) framework has been adopted for the control of small-amplitude perturbations in oscillator and amplifier flows. Examples of oscillator flows include, among others, supercritical flow over a shallow or deep cavity (Åkervik *et al.* 2007; Barbagallo, Sipp & Schmid 2009), flow over a shallow bump (Ehrenstein, Passaggia & Gallaire 2010) and flow past a flat plate (Ahuja & Rowley 2010). In all cases, stabilization of the flow by feedback control strategies could be accomplished. Amplifier flows are dominated by convective and transient processes, and successful control is defined by a marked reduction of the flow's inherent amplification potential. Control of amplifier flows using LQG techniques was first attempted for very idealized geometries (see e.g. Joshi, Speyer & Kim 1997; Bewley & Liu 1998; Chevalier *et al.* 2007), namely, in simple, one-dimensional configurations. For more complex and higher-dimensional flows, direct application of the LQG framework becomes prohibitively expensive, and reduced-order models have to be introduced for the practical design of the compensator. LQG-based compensators using reduced-order models have been applied by Bagheri, Brandt & Henningson (2009) to control the amplification of perturbations in a spatially developing boundary layer and by Ilak & Rowley (2008) to control transitional channel flow. In Bagheri & Henningson (2011), strong emphasis has been placed on the model reduction technology; in particular, it has been demonstrated that the

reduced-order model (ROM) had to capture accurately the input–output behaviour between actuators and sensors to ensure a positive compensator performance (Kim & Bewley 2007). Despite the first successful attempts at applying LQG-feedback control to amplifier flows, many questions remain open about the design and practical implementation of compensators for this type of flow. Owing to the flow’s tendency to amplify perturbations transiently, sensitivity becomes the key concept in the design and performance evaluation of compensators: sensitivity to sensor and actuator placement, to the accuracy of the ROM and to nonlinear effects. Some of these issues have been addressed using an idealized (parallel base flow) model problem in Ilak (2009); a comprehensive analysis of closed-loop control for amplifier flows, however, is missing.

The goal of the present study is an identification of the various environmental and procedural factors and the assessment of their influence on the performance of the compensator for a specific amplifier flow: the case of a two-dimensional, laminar flow over a rounded backward-facing step (see Blackburn, Barkley & Sherwin 2008; Marquet *et al.* 2008; Dergham *et al.* 2011). This configuration is characterized by a detachment of the flow close to the step, followed by a recirculation zone; even though the flow is globally stable, perturbations are amplified as they are convected along the shear layer. This is due to a Kelvin–Helmholtz type of instability, which creates a convectively unstable region, extending approximately from the detachment to the reattachment point. If upstream residual noise is present, for example white, Gaussian noise, the flow will be unsteady, with a broadband spectrum in the bubble. Our control objective consists in suppressing this unsteadiness using an optimal controller, which converts a measurement signal obtained from a wall-mounted sensor into a control law that is subsequently supplied to an actuator. We believe that the results obtained for this specific configuration also hold, at least qualitatively, for other convectively unstable flows, such as, for example, a supercritical boundary layer developing over a flat plate subject to Tollmien–Schlichting instabilities. A discussion about the similarities of and differences between these two configurations is postponed to § 2.

The present study is structured as follows. After a brief description of the flow configuration, its noise amplification behaviour and the basic principles of LQG control and model reduction (§ 2), we start by considering the estimation problem (§ 3) and address sensor placement and estimation speed. In § 4 the controller will be introduced, performance limitations of the compensator will be discussed and the influence of the choice of control objective will be assessed. Section 5 will present the application of the LQG controller to linearized numerical simulations; specifically, the sensitivity to model inaccuracies and its relation to stability margins for the compensated system will be treated, based on both classical stability concepts and worst-case optimization. In § 6 we apply linear control to a nonlinear simulation and discuss the validity range of the linear compensator. A summary of results and conclusions are given in § 7.

## 2. Configuration and mathematical model

### 2.1. Flow configuration and governing equations

We study the laminar and incompressible flow over a two-dimensional rounded backward-facing step, which is sketched in figure 1, together with the geometric measures, the base flow stream-function and the set-up of control inputs and sensor outputs. Only a reduced part of the computational domain is shown. The step height  $h$  and the inflow velocity  $U_\infty$  are chosen as the characteristic length and velocity scales

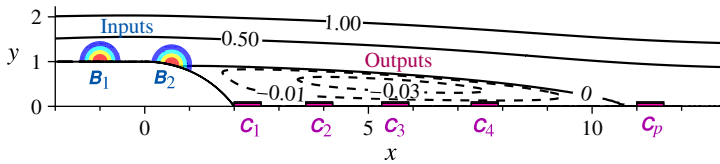


FIGURE 1. Sketch of the geometry for flow over a rounded backward-facing step, showing the stream-function of the base flow at  $Re = 600$  (dashed values refer to negative values). The stream-function is set to zero at the lower boundary of the computational domain. The upstream, downstream and top boundaries are respectively located at  $x = -20$ ,  $x = 100$  and  $y = 20$ . A typical mesh yields  $n = 400\,775$  degrees of freedom from 88 181 triangles. The positions of the input ( $B_{1,2}$ ) and output ( $C_{1,2,3,4,p}$ ) devices are also shown.

of the problem. The rounded part of the step consists of a circular arc extending from  $(x = 0, y = 1)$  to  $(x = 2, y = 0)$ . The flow enters the computational domain from the left (at  $x = -20$ ) with a constant streamwise velocity. A free-slip condition is imposed on the upstream part of the lower boundary ( $-20 \leq x \leq -2$ ,  $y = 1$ ), beyond which a laminar boundary layer starts to develop; no-slip conditions are enforced on the remaining lower boundary given by  $-2 \leq x \leq 100$ . On the top part of the computational domain, at  $y = 20$ , a symmetry condition is implemented, and a standard outflow condition is prescribed at the outlet ( $x = 100$ ). The symmetry and outflow boundary conditions have been placed far from the backward-facing step to ensure negligible influence of the choice of boundary conditions on the inherent flow dynamics.

The Reynolds number based on the step height and inflow velocity is chosen as  $Re = 600$  and held constant throughout our study. For this Reynolds number, the flow separates at  $x \approx 0.6$  and reattaches at  $x \approx 11$ , forming an elongated recirculation bubble. The displacement thickness of the incoming boundary layer at  $x = 0$  is equal to  $\delta^* \approx 0.082$ , which yields a Reynolds number based on the displacement thickness of  $Re_{\delta^*} \approx 49.2$ . The base flow, a solution of the nonlinear steady Navier–Stokes equations, is visualized by iso-contours of its stream-function in figure 1.

Flow over a rounded backward-facing step is a prototypical example for an amplifier flow since small upstream perturbations may be selectively amplified in the shear layer due to a Kelvin–Helmholtz instability (see next section for details). Characteristic unsteadiness arises from low-level noise via a linear amplification mechanism, which subsequently saturates nonlinearly once sufficiently high amplitudes have been reached. It is the goal of this paper to devise and assess an active feedback control strategy that decreases the convective amplification of random perturbations. We will consider small-amplitude noise; the dynamics of the perturbations is thus linear, which justifies using the Navier–Stokes equations linearized about the base flow as a mathematical model. The governing equations are spatially discretized using finite elements of Taylor–Hood type (P2–P2–P1) and implemented using the FreeFem++ software (see Hecht *et al.* 2005). In matrix form, these read

$$\mathbf{Q} \frac{d\mathbf{X}}{dt} = \mathbf{A}\mathbf{X}, \quad (2.1)$$

where  $\mathbf{X}$  denotes the state vector containing the velocity and pressure fields,  $\mathbf{A}$  represents the Navier–Stokes operator linearized around the base flow (shown in

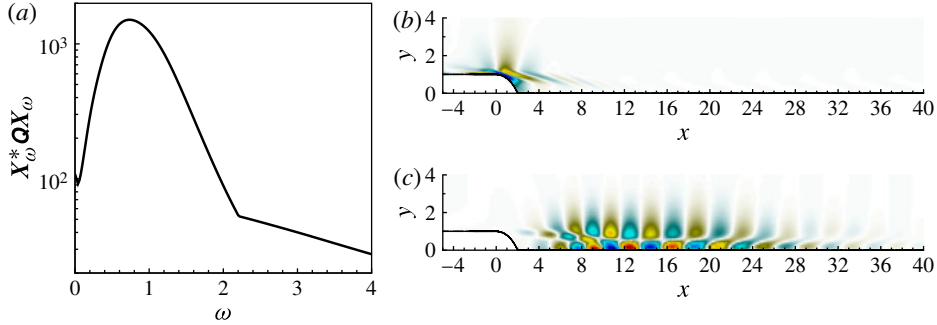


FIGURE 2. (a) Optimal energy response of the linear system to a harmonic forcing of frequency  $\omega$ . (b) Optimal forcing visualized by contours of the streamwise velocity. (c) Optimal response visualized by contours of the streamwise velocity.

figure 1) and  $\mathbf{Q}$  stands for the mass matrix, which simultaneously defines the perturbation kinetic energy according to  $E = \mathbf{X}^* \mathbf{Q} \mathbf{X}$ .

## 2.2. Noise amplification behaviour

For the chosen Reynolds number of  $Re = 600$ , the flow is globally stable and the matrix  $\mathbf{A}$  does not show any unstable eigenvalues. Yet, sustained unsteadiness may arise from the continuous excitation of the flow by upstream noise. This noise amplifier behaviour can be analysed and quantified in terms of the optimal harmonic forcing and its response in the frequency domain (see Alizard, Cherubini & Robinet 2009; Sipp *et al.* 2010). For a given frequency  $\omega$ , a periodic forcing of the form  $\mathbf{F}_\omega \exp(i\omega t)$  yields a corresponding response  $\mathbf{X}_\omega \exp(i\omega t)$ , where  $\mathbf{X}_\omega$  is given by  $\mathbf{X}_\omega = (i\omega \mathbf{Q} - \mathbf{A})^{-1} \mathbf{Q} \mathbf{F}_\omega$ . The optimal forcing is defined as the forcing  $\mathbf{F}_\omega$  of unit energy (i.e.  $\mathbf{F}_\omega^* \mathbf{Q} \mathbf{F}_\omega = 1$ ) that maximizes the energy of the response. The corresponding response  $\mathbf{X}_\omega$  is referred to as the optimal response; its energy  $\mathbf{X}_\omega^* \mathbf{Q} \mathbf{X}_\omega$  is the optimal energy gain due to external forcing at a prescribed frequency  $\omega$ . We will use the subscript  $\omega$  to indicate quantities defined in the frequency domain.

In figure 2(a), the optimal energy gain is presented as a function of the forcing frequency. The semi-logarithmic graph shows a parabolic curve, with the highest response to forcing around a frequency of  $\omega = 0.8$ . For frequencies above  $\omega \approx 2$ , the energy gain decays monotonically. In figure 2(b,c), the spatial shapes of the optimal forcing and response (real part only) taken at the highest energy gain are visualized by contours of the streamwise component. In accordance with the convective nature of the flow, we observe that the optimal forcing is concentrated upstream near the step, while the associated response is located further downstream. Hence, a noise source situated near the rounded step (mimicking an upstream, stochastic disturbance environment) can efficiently trigger perturbations whose maximum amplitudes are attained near  $x \approx 12$ . Based on this result, we model the noise as a Gaussian-shaped momentum forcing located at  $(x = -1, y = 1)$  with a width of 0.6. After discretization, this forcing appears in form of the matrix  $\mathbf{B}_1$  in the linear system

$$\mathbf{Q} \frac{d\mathbf{X}}{dt} = \mathbf{A} \mathbf{X} + \mathbf{Q} \mathbf{B}_1 w(t), \quad (2.2)$$

with  $w(t)$  describing the temporal behaviour of the noise. For the sake of simplicity, the noise will be taken as white in time with zero mean  $\langle w \rangle = 0$  and variance  $\langle w^2 \rangle$

denoted by  $W^2$ . We have chosen a compact source of disturbances located upstream in accordance with the physical conditions of advection-dominated flows. Even though an alternative global forcing by noise is conceivable, this particular set-up, besides running counter to the principal physical mechanisms, would not be amenable to effective flow control strategies owing to a poor sensing and estimation process. In addition, we assume that a linear model is sufficient in describing the flow behaviour; in this sense, we restrict ourselves to small-amplitude processes, as mentioned above.

In continuing to set up our flow control problem, an appropriate objective or cost functional has to be specified. To this end, two quantities will be considered. The first quantity consists of the shear stress measured at the wall and is computed following  $m_p = \mathbf{C}_p \mathbf{X} = \int_{x=1}^{x=11.6} \partial_y u' dx$ . The placement of this sensor has been motivated by the location of maximum response of the flow to harmonic excitation (see figure 2c). For higher frequencies ( $\omega > 2$ ), the optimal response moves upstream towards the detachment point and is no longer observable by the sensor  $\mathbf{C}_p$ ; for lower frequencies, the spatial support of the optimal response extends both upstream and downstream (with the most energetic region remaining near the reattachment point). Hence, sensor  $\mathbf{C}_p$  will detect all perturbation frequencies with  $\omega \leq 2$ . The second quantity of interest is the total kinetic perturbation energy contained in the entire domain; it is given by  $E = \mathbf{X}^* \mathbf{Q} \mathbf{X}$ . The control to be designed will aim at diminishing either  $m_p$  or  $E$ . It is interesting to note that, under random forcing, the two quantities of interest,  $m_p$  and  $E$ , display a frequency response strikingly similar to that given in figure 2(a); the spatial structure of the stochastic response resembles that given in figure 2(c) (the reader is referred to figure 9 for verification).

### 2.3. Linear quadratic Gaussian (LQG) control

A closed-loop control strategy is considered in order to weaken or suppress the amplification of perturbations. In contrast to open-loop control strategies, this method extracts information from the system via measurements, which is then processed to apply real-time actuation. This technique allows flow manipulation with rather low expended energy and permits the application and adaptation of control laws to a variety of flow situations, provided the model is representative of and robust to physical and parametric changes. The approach taken in our study is based on a compensator designed within the linear quadratic Gaussian (LQG) control framework (see Burl 1999). The actuator through which control efforts are exerted on the flow consists of a body force acting on the vertical momentum component; the location, shape and type of the actuator is summarized in the matrix  $\mathbf{B}_2$  (see figure 1). The control law  $u(t)$  that describes the temporal behaviour of the actuator is based on real-time measurements of the flow from sensors, which extract shear stresses and are located at various positions along the wall. The governing system of equations, including the actuators and sensors, can be cast into the familiar state-space form

$$\mathbf{Q} \frac{d\mathbf{X}}{dt} = \mathbf{A} \mathbf{X} + \mathbf{Q} \mathbf{B}_1 w + \mathbf{Q} \mathbf{B}_2 u, \quad m = \mathbf{C} \mathbf{X} + g(t), \quad (2.3)$$

where  $g(t)$  is a zero-mean measurement noise of variance  $G^2$ , which contaminates the measure  $m$ . The link between the measurement signal  $m$  and the actuation law  $u$  is provided by the compensator. Figure 3 presents a sketch of a typical LQG control set-up, including the system to be controlled as well as the two components of the compensator: the estimator and the controller. The module labelled ‘Plant’ represents our fluid system whose flow characteristics we wish to modify; it is given mathematically by (2.3). The plant depends on the initial condition  $\mathbf{X}(t_0)$ , the noise



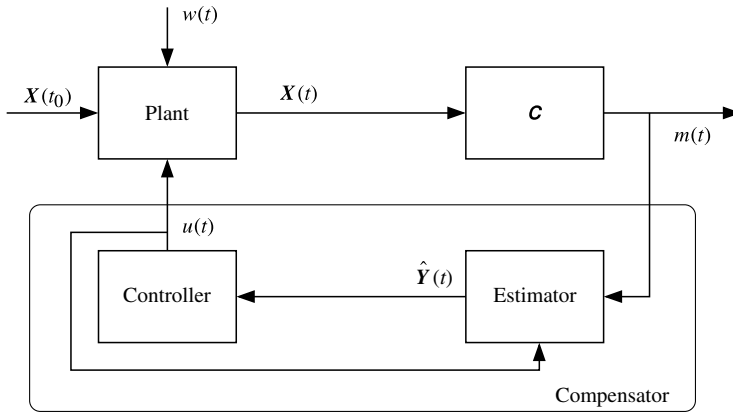


FIGURE 3. Sketch of a typical LQG control set-up.

input  $w(t)$  and the control law  $u(t)$ , and provides as an output the state vector  $X$ . A measurement signal  $m$  can be extracted at all times from the state vector, which is then passed to the compensator. In a first step, the estimator will reconstruct an estimated state  $\hat{Y}(t)$  from the measurement  $m$ , which is, in a second step, used by the controller to compute the control law  $u(t)$ . More details about the design of the estimator and the controller will be given below.

It is important to stress that the placement of the actuator and sensor is critical for the success of closed-loop control. In our case, the actuator is positioned near the separation point (see control input  $B_2$  in figure 1), which corresponds to the location where the optimal forcing structures are most prominent, independent of the frequency (see figure 2b, which illustrates the case for  $\omega = 0.8$ ). This placement optimally exploits the sensitivity of the flow to external forcing and suggests that low-amplitude control at this location may exert sufficient influence on the flow behaviour to accomplish our control objective. In other words, the chosen actuator location should ensure low control gains.

Analogously, the placement of the sensor requires care and thought. Commonly, measurements are taken at locations where the flow feature we wish to suppress is particularly prevalent. Recalling the spatial structure of the most amplified flow response to optimal forcing (see figure 2c), this would suggest a sensor placement downstream of the reattachment point near  $x \approx 12$ . Nevertheless, we will demonstrate that this particular choice does not yield an efficient and effective closed-loop control, and we will methodically explore the estimator performance based on sensors placed further upstream in the recirculation bubble (see figure 1). In particular, four discrete sensor locations, denoted by  $C_{1,2,3,4}$ , will be assessed; these are distinct from the performance sensor  $C_p$ .

More generally, to ensure low control gains and a physically relevant control objective, the actuator should be placed at the transition location from the stable to the convectively unstable flow regime (branch I) and the performance sensor  $C_p$  at the transition location from convectively unstable to the stable flow regime (branch II). Indeed, in a convectively unstable flow, the instability is cumulative in the downstream direction: branch I is the point where an action has largest effect on the perturbation, while branch II is the point where the perturbation is strongest. The locations of branches I and II usually depend on the frequency of the perturbation; in the present

flow over a backward-facing step, however, branches I and II are located for all frequencies near the flow separation and reattachment points (not shown here). Hence, a single actuator and a single performance sensor (plus one estimation sensor) are sufficient to stabilize the flow for all frequencies. In the case of a convectively unstable boundary layer developing over a flat plate, the locations of branches I and II strongly depend on the perturbation frequency. Hence, multiple input–output triplets (each consisting of actuator, performance sensor and estimation sensor) are necessary, where each triplet is designed to stabilize the flow in a bounded area in the downstream direction and in a restricted frequency band.

#### 2.4. Reduced-order model based on proper orthogonal decomposition

The design of the estimator and controller involves the numerical solution of two Riccati equations for the Kalman and control gain, respectively. The numerical effort is proportional to the dimension of the system matrix  $\mathbf{A}$ , which makes the direct solution of the Riccati equation excessively expensive or even impossible. It is thus necessary and common practice to substitute the full system by an equivalent system of considerably smaller dimensions and to compute the two gains based on this ROM of the flow. A standard technique to arrive at a ROM of the flow uses a Galerkin projection of the governing equations onto proper orthogonal decomposition (POD) modes (see Sirovich 1987). This method proves to be efficient (see Bagheri *et al.* 2009; Barbagallo *et al.* 2009; Bagheri & Henningson 2011) in capturing the main characteristics of the original system required for closed-loop control, namely the dynamics between the inputs (given by  $\mathbf{B}_1$  and  $\mathbf{B}_2$ ) and the outputs (given by  $\mathbf{C}_{1,2,3,4}$  and the control objectives  $E$  and  $\mathbf{C}_p$ ). The governing equation for the ROM is similar to (2.3) and is given by

$$\frac{d\hat{\mathbf{X}}}{dt} = \hat{\mathbf{A}}\hat{\mathbf{X}} + \hat{\mathbf{B}}_1 w + \hat{\mathbf{B}}_2 u, \quad m = \hat{\mathbf{C}}\hat{\mathbf{X}}, \quad (2.4)$$

where the superscript ‘hat’ indicates reduced quantities. The energy of the state  $E$  is simply given by  $\|\hat{\mathbf{X}}\|^2 = \hat{\mathbf{X}}^* \hat{\mathbf{X}}$ , since the projection basis is orthonormal with respect to the energy inner product. The use of a ROM decreases the dimension of our system from  $O(10^6)$  to  $\sim 150$  degrees of freedom and thus allows the application of standard direct algorithms for LQG control design. The choice of POD modes as a projection basis has essentially been motivated by the requirement for capturing the energy output. A standard balanced-truncation technique (see Bagheri *et al.* 2009; Barbagallo *et al.* 2009; Ahuja & Rowley 2010) is not able to cope with large-dimensional outputs, unless the ‘output projection technique’ is used (Rowley 2005); this technique however is beyond the scope of this study. Accounting for disturbances in the entire flow domain would require a ROM capturing the entire input space. Since our goal is to target the kinetic energy of the perturbations, we need to represent the full output space accurately. This choice prohibits the consideration of disturbances in the entire flow domain, since standard model-reduction techniques are not capable of dealing with both large-scale input and large-scale output spaces. A comparison between the transfer function from  $u$  to  $m_1$  of the linearized direct numerical simulation (DNS) and the ROM based on 150 POD modes is displayed in figure 4(a). It shows excellent agreement for frequencies in the range  $0 \leq \omega \leq 4$ . For larger frequencies, small discrepancies appear; the absolute error, however, remains below  $3 \times 10^{-3}$ . It is noteworthy that the maximum absolute error occurs at a frequency of  $\omega \approx 1$ , rather than at higher frequencies. In appendix A, we show that all transfer functions from



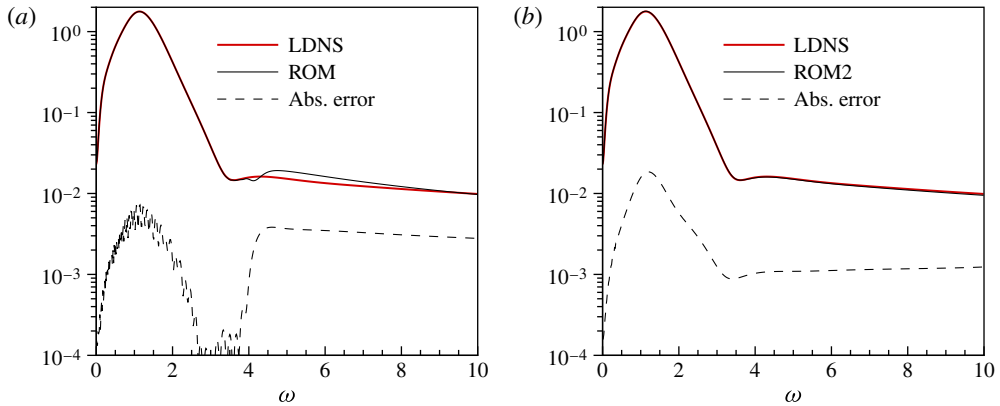


FIGURE 4. (Colour online available at [journals.cambridge.org/flm](http://journals.cambridge.org/flm)) (a) Transfer functions from  $u$  to  $m_1$  of the linearized DNS and the ROM based on 150 POD modes versus frequency  $\omega$ . The absolute error between the two transfer functions is included as the dashed line. (b) Same for a ROM based on 550 POD modes.

$w$  and  $u$  to  $m_{1,2,3,4,p}$  and  $E(t)$  can be captured with an  $\mathcal{H}_2$  error of less than 1%. This error seems quite small, which, at first glance, should ensure that a study of compensated systems with the ‘ROM as a plant’ is representative of compensated systems with the ‘linearized DNS as a plant’. This point of view is taken in § 3 for the estimation problem and in § 4 for the complete estimation–control problem. The above-mentioned error of 1% is nonetheless appreciable, and § 5 is thus devoted to the question whether this 1% error between the linearized simulation and the POD model is sufficiently small to guarantee in all cases the equivalence between a ROM-based and a linearized DNS-based study of the compensated system. In fact, one of the objectives of the present paper is to assess quantitatively the performance robustness of the compensator. Such issues become even more pertinent under more realistic conditions (e.g. in experimental realizations), as errors inevitably corrupt the quality of a ROM. It is essential to understand the minimum requirements on the quality of the ROM for acceptable or required control performance; it is equally essential to know how the compensated system will fail if these requirements are not met. In addition, should specific inputs and/or outputs be more accurately captured than others? In what follows we will try to address some of these points.

### 2.5. Validation of the reduced-order model

Since the objective of this paper is a study of performance robustness with respect to sensor placement, signal-to-noise ratios and control-cost parameters – all of which is accomplished based on a ROM – it is important to eliminate influences stemming from the truncation of the expansion basis for the underlying ROM. To this end, we have computed a ROM model using 550, rather than 150, POD modes. This extended model is able to capture accurately the exact input–output behaviour beyond the above-mentioned frequency of  $\omega \approx 4$  with an absolute error below  $10^{-3}$  for  $\omega \geq 3$ . The transfer function from  $u$  to  $m_1$  for this extended model is shown in figure 4(b). Higher frequencies are more accurately represented, compared to the 150-mode model, with a reduced absolute error. Each of the performance analyses that follow in the subsequent sections of this paper (with the exception of the internal stability margins in figure 14; the internal stability margins have only been recomputed for specific

parameters, cases 1–4, see below) have been recomputed to ensure results that are independent of the ROM's truncation error and to confirm the conclusions drawn in the text. This exercise proved that our working model (based on 150 POD modes, as described above) is more than adequate to yield converged results and to provide confidence in our conclusions.

### 3. Estimation and sensor placement

As a first step of the full control design and performance evaluation process, we concentrate on the estimator, in particular its performance with respect to the location of the sensors. We would like to reiterate that our analysis is based on the ROM introduced in the previous section.

#### 3.1. Presentation of the estimator

In general, the estimator's task is the approximate reconstruction of the full state vector using only limited information from the measurement. This approximate state vector will then be used by the controller to determine a control strategy that accomplishes our objective. The estimated state  $\hat{Y}$  is assumed to satisfy a set of equations similar to that governing the original system (2.4). We have

$$\frac{d\hat{Y}}{dt} = \hat{A}\hat{Y} + \hat{B}_2u(t) - \hat{L}(m - \hat{C}\hat{Y}), \tag{3.1}$$

where the original noise term  $\hat{B}_1w(t)$  has been replaced by the forcing term  $-\hat{L}(m - \hat{C}\hat{Y})$ . The latter term represents the difference between the true measurement signal  $m(t) = \hat{C}\hat{X}$  and the estimated measurement signal  $\hat{C}\hat{Y}$  and is applied as a forcing term premultiplied by  $\hat{L}$ . This term is to drive the estimated state  $\hat{Y}$  towards the true state  $\hat{X}$ . In the forcing term, the so-called *Kalman gain*  $\hat{L}$  can be computed from an optimization problem in which the cost functional is taken as the error between the full and estimated states, i.e.  $\hat{Z} = \hat{X} - \hat{Y}$ , and is subsequently minimized. The resulting optimality condition yields a Riccati equation, from which the Kalman gain  $\hat{L}$  follows (see Burl 1999). Commonly, the energy of the estimation error is formulated in the time domain; it will prove advantageous in our case, though, to recast the energy in the frequency domain. Using Parseval's theorem we obtain for the objective functional

$$\bar{Z} = \int_{-\infty}^{\infty} \|\hat{Z}_\omega\|^2 d\omega, \tag{3.2}$$

where  $\hat{Z}_\omega$  denotes the Fourier transform of the error  $\hat{Z}$ . Two sources of noise – both assumed as white in time – are taken into account in the derivation and solution of the Riccati equation: a plant noise  $w(t)$  of variance  $W^2$  driving the dynamics of the original system (2.4) and a measurement noise  $g(t)$  with variance  $G^2$  contaminating the measurement  $m(t)$ . The ratio of the two standard deviations, i.e.  $G/W$ , can be taken as a parameter that governs the speed of the estimation process, but can also be interpreted as the noise-to-signal ratio of the sensor. For example, considering a constant standard deviation  $W$  of the plant noise, the parameter  $G/W$  represents a quality measure of the sensor. Large values of  $G/W$  indicate that the measurement noise  $g(t)$  is too high to ensure a correct signal; the corresponding Kalman gain  $\hat{L}$  tends to zero. Consequently, the forcing term in (3.1) has a negligible effect on the

system, which, in turn, leads to a poorly performing estimator. This parameter regime is referred to as the small-gain limit (SGL). Contrary to the small-gain limit, for  $G/W \ll 1$  the corruption of the measurement signal by noise is low compared to the stochasticity arising from the system itself. As a consequence, the estimation process becomes highly effective owing to the substantial Kalman gains. This parameter regime, referred to as the large-gain limit (LGL), comprises the most performing estimators for a given configuration.

By construction, the performance of the estimator crucially depends on details related to the measurement signal, and the type of sensor (in terms of its noise-to-signal ratio) as well as its location have to be chosen judiciously if overall success of the closed-loop control effort is to be expected. In what follows, we will consider four sensors  $\hat{\mathbf{C}}_{1,2,3,4}$  that are identical in type but placed at four different positions within the recirculation bubble, and assess their capability of efficiently estimating the flow state.

### 3.2. Performance of the estimator

In this section, we further elaborate on estimating the flow state  $\hat{\mathbf{X}}$  governed by (2.4). The estimation problem is decoupled from the control problem (see Burl 1999). For this reason, we can set the control law to zero ( $u(t) = 0$ ) without loss of generality and continue our study of the estimation problem without actuation. The system is driven by white noise represented by  $w(t)$ ; but, owing to the linearity of (2.4), the performance of the estimator can equivalently be studied by considering harmonic forcings  $w(t) = \exp(i\omega t)$  of a given frequency  $\omega$ . It is then convenient to reformulate the coupled plant–estimator system in the frequency domain and state the governing equations for the harmonic response as

$$\begin{pmatrix} \hat{\mathbf{X}}_\omega \\ \hat{\mathbf{Y}}_\omega \end{pmatrix} = \begin{pmatrix} i\omega I - \hat{\mathbf{A}} & \hat{\mathbf{0}} \\ \hat{\mathbf{L}}\hat{\mathbf{C}} & i\omega I - (\hat{\mathbf{A}} + \hat{\mathbf{L}}\hat{\mathbf{C}}) \end{pmatrix}^{-1} \begin{pmatrix} \hat{\mathbf{B}}_1 \\ \hat{\mathbf{0}} \end{pmatrix}, \quad (3.3)$$

where, as before, the subscript  $\omega$  indicates variables defined in the frequency domain. The estimation error in frequency space is given as  $\hat{\mathbf{Z}}_\omega = \hat{\mathbf{X}}_\omega - \hat{\mathbf{Y}}_\omega$ .

In figure 5(a) the frequency dependence of the estimation error  $\|\hat{\mathbf{Z}}_\omega\|^2$  is displayed for the shear-stress sensor placed at  $\mathbf{C}_1$  (see figure 1) and for selected values of the noise-to-signal parameter  $G/W$ . For comparison, the norm of the state vector  $\|\hat{\mathbf{X}}_\omega\|^2$ , which is similar to figure 2(a), is included as a dashed line. In the small-gain limit (red line), the estimator, as expected, does not succeed in identifying the state, producing an error as large as the norm of the original state. As the parameter  $G/W$  decreases though, the estimation process improves due to a less contaminated input from the sensors, and the estimation error is reduced – mainly at frequencies where the system reacts strongly to external excitations. As the parameter  $G/W$  approaches the large-gain limit (blue lines), the error curve eventually converges to the lowest possible value. This curve then defines the best attainable performance for sensor  $\hat{\mathbf{C}}_1$ .

This general behaviour is observable for each of the four sensors (not shown here). The final errors in the large-gain limit, however, are not identical for all sensors: the best performance is achieved by sensor  $\hat{\mathbf{C}}_1$ . As the location of the sensor is moved further downstream in the separation bubble (considering successively the sensors  $\hat{\mathbf{C}}_1$ ,  $\hat{\mathbf{C}}_2$ ,  $\hat{\mathbf{C}}_3$  and  $\hat{\mathbf{C}}_4$ ), the frequencies that are naturally amplified by the system are less well predicted.

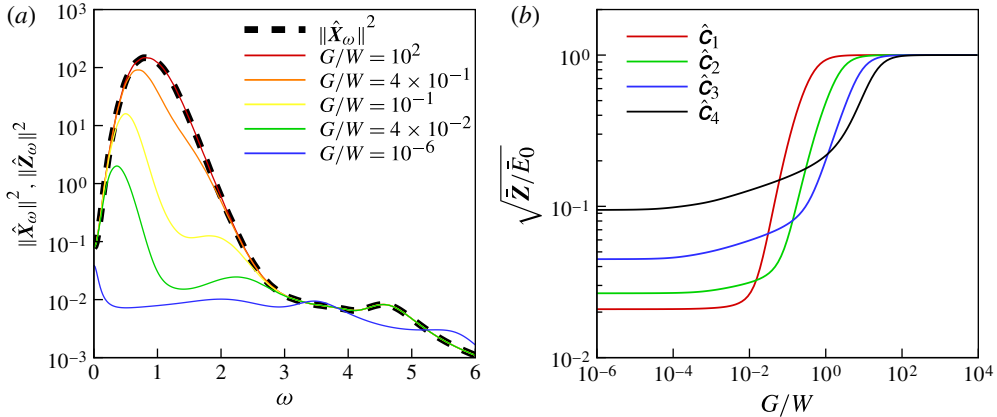


FIGURE 5. Performance of the estimator versus frequency using four different sensors and selected values of the estimation (noise-to-signal) parameter  $G/W$ . (a) Sensor  $\hat{\mathbf{C}}_1$ ; normalized performance of the estimator, integrated over all frequencies, versus the estimation parameter  $G/W$  for four different sensor locations. (b) Measuring shear stress.

An instructive way of assessing the performance of an estimator over all frequencies is to directly compute the cost functional  $\bar{\mathbf{Z}}$  (see (3.2)) normalized by the energy of the state. We thus introduce  $\sqrt{\bar{\mathbf{Z}}/\bar{E}_0}$ , with  $\bar{E}_0 = \int_{-\infty}^{\infty} \|\hat{\mathbf{X}}_\omega\|^2 d\omega$  and  $\hat{\mathbf{X}}_\omega = (i\omega\mathbf{I} - \hat{\mathbf{A}})^{-1} \hat{\mathbf{B}}_1$ . When this quantity is close to 1, the estimation process has failed with a 100% estimation error; the smaller the value, the better performing the estimator. This quantity is displayed in figure 5(b) versus the estimation parameter  $G/W$  for each of the four sensors. The red curve represents the estimator performance based on sensor  $\hat{\mathbf{C}}_1$ . For this sensor location and for noise-to-signal ratios above 1, the sensor noise prohibits a correct estimation, resulting in an estimation error of 100%. As the noise-to-signal ratio diminishes further, the performance of the estimator progressively increases until it reaches the large-gain limit for values of  $G/W$  less than approximately  $10^{-2}$ . Below this value of  $G/W$ , the estimator performs at its optimum. Similar behaviour can be observed for the remaining sensor locations given by  $\hat{\mathbf{C}}_2$ ,  $\hat{\mathbf{C}}_3$  and  $\hat{\mathbf{C}}_4$ : the small-gain limit regime is clearly detectable at high values of  $G/W$ . However, the exact values for which the estimator reaches the large-gain limit become less sharply defined as the sensor location is moved further downstream in the separation bubble. Comparing the performance of estimators based on different sensors, we conclude, in agreement with figure 5, that the performance in the large-gain limit is best for the sensor  $\hat{\mathbf{C}}_1$  and decreases as the sensor is moved further downstream. It is surprising, though, that the estimator based on  $\hat{\mathbf{C}}_4$ , which performs worst in the large-gain limit, shows better performance at high values of the noise-to-signal ratio  $G/W$ . For example, if we consider the value  $G/W = 10^0$ , the estimator based on  $\hat{\mathbf{C}}_4$  displays a relative error of 20% while the estimator based on  $\hat{\mathbf{C}}_1$  still shows an error of 100%. If a constant noise level of the system-generated signal is assumed ( $W = \text{const.}$ ), this implies that the estimator based on  $\hat{\mathbf{C}}_4$  can cope with higher levels of measurement noise than the estimator based on  $\hat{\mathbf{C}}_1$ . In practice, this means that lower-quality sensors can be used as long as they are placed further downstream; this point will be discussed further in the next section.

---

Sensor	$W'/W$	$G/W _{SGL}$	$G/W _{MGL}$	$G/W' _{SGL}$	$G/W' _{MGL}$
1	0.14	1.25	0.21	8.9	1.5
2	0.31	6.4	1	10.5	1.64
3	1.87	21	3.5	11.2	1.87
4	4	52	7	13	1.75

---

TABLE 1. Estimation parameters  $G/W$  and true noise-to-signal ratios  $G/W'$  for the four sensors  $\hat{\mathbf{C}}_{1,2,3,4}$  in the small-gain limit (SGL) and medium-gain limit (MGL). The critical values for the small-gain limit are based on  $\sqrt{\bar{\mathbf{Z}}/\bar{E}_0} = 0.95$ ; the critical values for the medium-gain limit are based on  $\sqrt{\bar{\mathbf{Z}}/\bar{E}_0} = 0.5$ . Values for  $W'/W$  may be obtained by inspection of the impulse responses (see figure 7).

---

It seems fitting to mention here that, although the term  $G/W$  parametrizes the performance quantities via the governing equations, a more intuitive and physically relevant quantity is the ratio of the sensor noise variance  $G$  to a measure of the noise covariance localized near the sensor location. Denoting the actual amplitude of the signal detected by the sensor by  $W'$ , we can define the true noise-to-signal ratio  $G/W'$ . Values for all four sensors are presented in the second column of table 1. We proceed by introducing the small-gain limit (SGL) at a threshold value of  $\sqrt{\bar{\mathbf{Z}}/\bar{E}_0} = 0.95$  and a medium-gain limit (MGL) at a threshold value of  $\sqrt{\bar{\mathbf{Z}}/\bar{E}_0} = 0.5$  and determine, for all four sensors, critical values of the true noise-to-signal ratio  $G/W'$  for the estimation process using  $G/W' = (G/W)/(W'/W)$ . Values for  $W'/W$  can be determined by analysing the maximum measurement amplitudes  $m$  from a simulation starting with an impulse at  $\mathbf{B}_1$  (see figure 7 for example). Referring back to figure 5(b) for results on sensor  $\hat{\mathbf{C}}_1$ , we observe that estimation becomes effective for  $G/W < 1.25$ , which corresponds to  $G/W' < 8.9$ . Analogous results for the other sensors are reported in table 1. It appears that the estimation process for each of the four sensors starts being efficient for values of the true noise-to-signal ratio  $G/W' \approx 10$ , i.e. when the magnitude of the signal from the plant (measured by  $W'$ ) is 10 times smaller than the noise intrinsic to the sensor (measured by  $G$ ). If  $G/W'$  is of order one (see sixth column of table 1), the estimation process performs significantly better: the estimation performance parameter in figure 5(b) has reached the mean value between the small-gain limit performance (unity for all sensors) and the large-gain limit performance (e.g. 0.02 for sensor  $\hat{\mathbf{C}}_1$ ). Optimal performance is obtained for true noise-to-signal ratios  $G/W'$  of the order of  $10^{-2}$ .

To conclude, the estimation errors are rather small ( $< 10^{-1}$ ) for all sensors in the large-gain limit. Yet, the estimator based on  $\hat{\mathbf{C}}_1$  is most efficient, with a performance measure of  $2 \times 10^{-2}$ , while the estimator based on  $\hat{\mathbf{C}}_4$  only reaches a value of  $10^{-1}$  in the large-gain limit. At first glance, this difference in performance may seem small and insignificant, but it will be shown below (§ 4) that it nonetheless has a strong influence on the efficiency of the compensator. But first, the next section will offer a physical explanation for the observed loss of estimation performance by analysing the above results in the time domain rather than the frequency domain.

### 3.3. Interpretation in the time domain

Even though a formulation of the estimation problem in the frequency domain is the proper choice for designing closed-loop control strategies for open flows, it

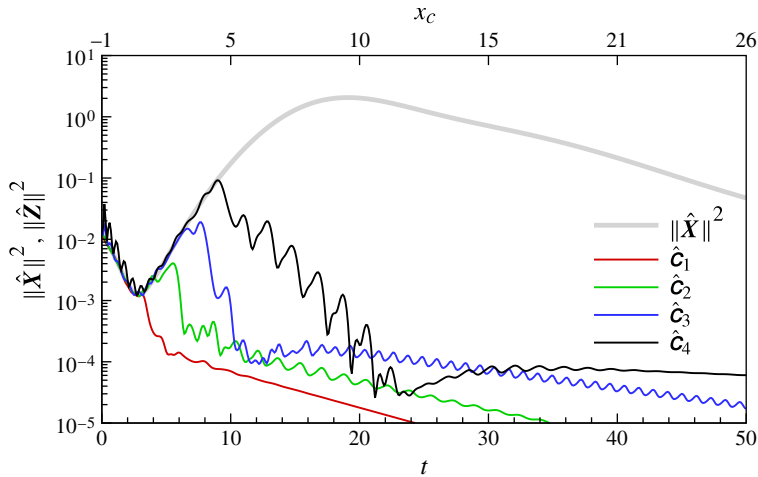


FIGURE 6. Temporal evolution of the energy of the error vector  $\|\hat{\mathbf{Z}}\|^2$  for four different sensor locations  $\hat{\mathbf{C}}_{1,2,3,4}$ , and energy of the (uncontrolled) state  $\|\hat{\mathbf{X}}\|^2$  (in grey).

nevertheless remains challenging to attach physical meaning to the frequency-based results; an interpretation of our findings in the time domain seems more intuitive. The main result – the estimator’s performance deteriorates as the sensor is gradually moved from the upstream  $\hat{\mathbf{C}}_1$  to the downstream  $\hat{\mathbf{C}}_4$  position – suggests that the travel time of a perturbation, before it is detected by the sensor, plays a critical role. To validate this proposition, we start by rewriting the estimation performance parameter in the time domain using Parseval’s theorem. We obtain  $\int_{-\infty}^{\infty} \|\hat{\mathbf{Z}}_{\omega}\|^2 d\omega = 2\pi \int_0^{\infty} \|\hat{\mathbf{Z}}\|^2 dt$ , with  $\hat{\mathbf{Z}} = \hat{\mathbf{X}} - \hat{\mathbf{Y}}$ , and  $\hat{\mathbf{X}}$  and  $\hat{\mathbf{Y}}$  satisfying the following system of equations in the time domain:

$$\frac{d}{dt} \begin{pmatrix} \hat{\mathbf{X}} \\ \hat{\mathbf{Y}} \end{pmatrix} = \begin{pmatrix} \hat{\mathbf{A}} & \hat{\mathbf{0}} \\ -\hat{\mathbf{L}}\hat{\mathbf{C}} & \hat{\mathbf{A}} + \hat{\mathbf{L}}\hat{\mathbf{C}} \end{pmatrix} \begin{pmatrix} \hat{\mathbf{X}} \\ \hat{\mathbf{Y}} \end{pmatrix}, \quad \begin{pmatrix} \hat{\mathbf{X}} \\ \hat{\mathbf{Y}} \end{pmatrix}_{t=0} = \begin{pmatrix} \hat{\mathbf{B}}_1 \\ \hat{\mathbf{0}} \end{pmatrix}. \quad (3.4)$$

The above system determines an impulse response triggered by the noise term  $\hat{\mathbf{B}}_1$ : the initial condition  $\hat{\mathbf{X}}_{t=0} = \hat{\mathbf{B}}_1$  is advected downstream while being amplified along the shear layer of the recirculation bubble. The energy  $\|\hat{\mathbf{X}}\|^2$  of this perturbation is displayed versus time by the thick grey line in figure 6. In addition to the time axis, a second axis is displayed at the top of the figure where the location of the advected wave packet, evaluated by the energy-weighted  $x$  centroid  $x_c$  defined as  $x_c(t) = \int x k'(x, y, t) dx dy / \int k'(x, y, t) dx dy$  with  $k'(x, y, t) = (u'^2 + v'^2)/2$  as the pointwise kinetic energy at time  $t$ , is shown. The initial condition is associated with the non-zero state energy  $\|\hat{\mathbf{X}}\|^2 = \|\hat{\mathbf{B}}_1\|^2$  at  $t = 0$ . The energy then decreases for  $0 < t \lesssim 1.5$  as the perturbation traverses the stable region of the flow between the noise location and the separation point. Beyond the separation point of the shear layer, the wave packet enters the convectively unstable region and its energy grows until the perturbation reaches the attachment point. At time  $t \approx 19$  the energy reaches a maximum; the corresponding energy-weighted  $x$  centroid  $x_c$  is located at  $x \approx 9.5$ . The perturbation continues through a convectively stable region and the state energy



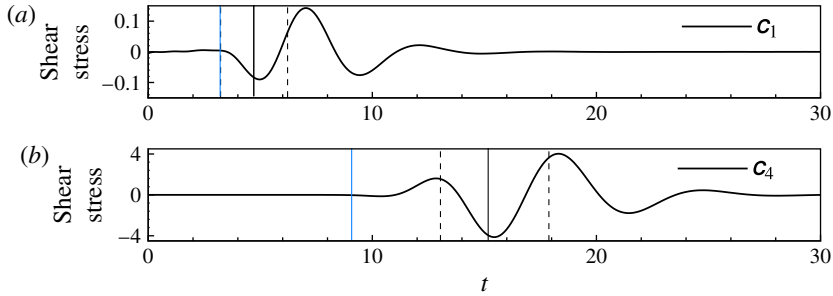


FIGURE 7. (Colour online) Measured impulse response at the four sensor locations,  $\hat{\mathbf{C}}_{1,4}$  (top to bottom). The solid grey (blue online) vertical lines correspond to the times when the curves in figure 6 deviate from  $\|\hat{\mathbf{X}}\|^2$ . The solid black vertical lines indicate the times when the energy-based  $x$  centroid of the wave packet  $x_c$  reaches the sensor. The dashed black vertical lines give the times when  $x_c \pm \sigma$  reaches the sensor, with  $\sigma$  denoting the standard deviation of the wave packet.

decreases accordingly. During this advective process, the estimator tries, in real time, to reconstruct the actual state from the information provided by one sensor, and the estimation performance parameter is given by the integral in time of the actual estimation error  $\hat{\mathbf{Z}}$ . In the following analysis, all estimators ( $\hat{\mathbf{C}}_1$  to  $\hat{\mathbf{C}}_4$ ) will operate at their respective large-gain limit, which ensures the best attainable performance for each estimator.

In figure 6 the thin solid lines display the energy of the estimation error  $\|\hat{\mathbf{Z}}\|^2$  as a function of time for all four sensors. The red curve traces the estimation error associated with sensor  $\hat{\mathbf{C}}_1$ . For short times ( $0 < t \lesssim 3$ ), the estimation error energy is comparable to the state energy, indicating a relative estimation error of 100%. Starting at  $t \approx 3$ , the error drops abruptly by one order of magnitude before a more gradual decrease sets in for  $t \gtrsim 6$ . The estimator becomes effective as soon as the error curve clearly detaches from the state energy curve (thick grey solid line); the state is hence well estimated beyond  $t \approx 4$  using sensor  $\hat{\mathbf{C}}_1$ . The estimation error curves (green, blue and black curves) for the remaining sensors  $\hat{\mathbf{C}}_{2,3,4}$  display a similar behaviour: a relative estimation error of 100% for early times, followed by a pronounced drop after a critical time and finally a gradual decay. The abrupt decline in the estimation error energy, however, occurs considerably later than for sensor  $\hat{\mathbf{C}}_1$ , and this delay increases steadily as the sensor location is moved further downstream. Nevertheless, in all cases the estimation error ultimately decreases, and the flow state appears to be well estimated for large times. We thus conclude that the principal difference between the estimators is the time at which they start to become effective: sensor  $\hat{\mathbf{C}}_1$ , located furthest upstream, yields the earliest accurate estimates of the state, followed by  $\hat{\mathbf{C}}_2$ ,  $\hat{\mathbf{C}}_3$  and finally  $\hat{\mathbf{C}}_4$ .

More insight is gained by displaying the measurements from the different sensors for the above impulse-response simulation (see figure 7). For sensor  $\hat{\mathbf{C}}_1$  (figure 7a) we observe a quiet phase ( $0 < t \lesssim 4$ ), after which a sinusoidal signal, the footprint of the wave packet travelling downstream in the shear layer above the sensor, is detected. The measurement returns to zero for  $t \gtrsim 16$ . Similar features can be observed for the other three sensors and in particular for sensor  $\hat{\mathbf{C}}_4$  (figure 7b). However, the

time of first detection is delayed and the amplitude of the signal is substantially increased (by nearly 40 times between  $\hat{\mathbf{C}}_1$  and  $\hat{\mathbf{C}}_4$ ) as we move the sensor location further downstream. The time delay in detecting the wave packet is closely linked to the overall performance of the four estimators: early detection yields better results. The detection times in figure 7 (blue vertical bars) correspond to the critical times in figure 6. After the wave packet has been captured by the sensor, the estimation proceeds rapidly due to the large Kalman gains (large-gain limit). If noise is generated at  $\hat{\mathbf{B}}_1$ , the  $\hat{\mathbf{C}}_4$  estimator, for example, is able to identify the associated response in the region  $x > 5$  but is incapable of detecting any response in the region  $-1 < x < 5$ . The performance of the estimator is thus determined less by the quality of the reconstructed state – all energy curves in figure 6 tend to zero – than by its reaction time, which translates into a spatial range where state responses to noise are detectable. It is this distinction that will have a marked impact on the performance of closed-loop control (see § 4) and will reveal the effectiveness of seemingly performing estimators when incorporated into a compensator.

Larger amplitudes are detected at sensors located further downstream, which stems from the amplification of the wave packet due to a convective instability along the shear layer of the separation bubble; the four sensors  $\hat{\mathbf{C}}_{1,2,3,4}$  capture the wave packet at various stages of this instability. This difference in amplitude also explains some features observed in figure 5(b). Comparing the curves associated with the different sensors  $\hat{\mathbf{C}}_{1,2,3,4}$ , we note that the estimation process becomes effective for different values of the noise-to-signal ratio  $G/W$ . For example, sensor  $\hat{\mathbf{C}}_1$  starts to perform well for  $G/W < 1.25$ , while sensor  $\hat{\mathbf{C}}_4$  only requires  $G/W < 52$ , which leads us to conclude that higher-quality sensors are required when one plans to place them further upstream where signals are generally weaker.

In summary, two competing mechanisms have been isolated in the estimation process for flow over a backward-facing step: (i) for an effective estimator, the sensor has to be located sufficiently upstream to allow a *rapid* identification of the perturbation; and (ii) on the other hand, the noise-to-signal ratio  $G/W$  has to be sufficiently small to enable an *accurate* estimate, thus favouring or forcing the placement of noisy sensors further downstream where the signal amplitudes are higher. In short, a balance between speed and accuracy of the estimation process has to be struck. Whereas the upstream placement of the sensors runs somewhat counter to the intuitive placement of the sensor near the reattachment line, it will be shown that, for our prototypical configuration, the speed of estimation appears more critical for a successful compensator performance than the capture of highly accurate measurements.

#### 4. Closed-loop control based on reduced-order model

After our analysis of the estimator and its performance, we now direct our attention to the complete compensator. After a brief presentation of the controller and its design steps, we investigate the performance of the compensator built on the four sensors  $\hat{\mathbf{C}}_{1,2,3,4}$ . Two objective functionals for the controller will be studied: (i) the square of the measurement based on  $\hat{\mathbf{C}}_p$  and integrated over time; and (ii) the time integral of the entire perturbation energy. Within this section, the plant is modelled by the ROM introduced in § 2.

#### 4.1. Presentation of the controller

We will aim at suppressing perturbations in our fluid system by employing an optimal control strategy, which will be designed to minimize a predefined cost functional. In mathematical terms, a control law of the form  $u(t) = \hat{\mathbf{K}}\hat{\mathbf{X}}$  will be assumed, where the control gain  $\hat{\mathbf{K}}$  arises from the solution of a Riccati equation (see Burl 1999). Traditionally, the cost functional is related to a quantity measuring the energy of the state, but also takes into account the control effort in terms of its expended energy.

In our study, two measures of the state will be considered in the minimization process: the energy contained in the measurement extracted at location  $\hat{\mathbf{C}}_p$  (see figure 1), yielding a cost functional of the form

$$J_m = \int_0^\infty (\hat{\mathbf{X}}^* \hat{\mathbf{C}}_p^* \hat{\mathbf{C}}_p \hat{\mathbf{X}} + l^2 u^2) dt, \quad (4.1)$$

or the perturbation energy contained in the entire domain, leading to a cost functional of the form

$$J_e = \int_0^\infty (\hat{\mathbf{X}}^* \hat{\mathbf{X}} + l^2 u^2) dt. \quad (4.2)$$

The parameter  $l$  appears in either choice and is referred to as the cost of control, as it quantifies the user-specified weighting of the control energy compared to the quantity to be minimized. Similar to the estimator, a small-gain limit (respectively, large-gain limit) parameter regime exists where the controller exerts nearly no action (respectively, maximum action) on the flow. Invoking the separation principle (see Burl 1999), the controller design can be carried out independently of the estimator design.

The performance assessment of the compensator will follow the frequency-based framework outlined in §§ 2 and 3. Considering the state-space system (2.4) driven by a harmonic excitation  $w(t) = \exp(i\omega t)$ , the response of the compensated system reads

$$\begin{pmatrix} \hat{\mathbf{X}}_\omega \\ \hat{\mathbf{Y}}_\omega \end{pmatrix} = \begin{pmatrix} i\omega \mathbf{I} - \hat{\mathbf{A}} & -\hat{\mathbf{B}}_2 \hat{\mathbf{K}} \\ \hat{\mathbf{L}} \hat{\mathbf{C}} & i\omega \mathbf{I} - (\hat{\mathbf{A}} + \hat{\mathbf{B}}_2 \hat{\mathbf{K}} + \hat{\mathbf{L}} \hat{\mathbf{C}}) \end{pmatrix}^{-1} \begin{pmatrix} \hat{\mathbf{B}}_1 \\ \hat{\mathbf{0}} \end{pmatrix}. \quad (4.3)$$

The above equation will form the basis for our performance analysis of the compensated system, where we will focus on the influence of controllers designed with  $J_m$  or  $J_e$  as well as on the impact of the control cost  $l$  and the noise-to-signal ratio  $G/W$ .

#### 4.2. Performance of the compensator using a cost functional based on the measurement

We start by considering a compensator whose controller has been designed using the cost functional  $J_m$ , i.e. the state is measured by the energy output of the sensor  $\hat{\mathbf{C}}_p$  and the resulting controller aims at minimizing the energy of the measurement  $m_p = \hat{\mathbf{C}}_p \hat{\mathbf{X}}$ .

##### 4.2.1. Effect on the perturbation measure $m_p$

Figure 8(a,b) shows the performance of the compensator designed to minimize the measurement using, respectively, sensors  $\hat{\mathbf{C}}_1$  and  $\hat{\mathbf{C}}_4$  for the estimator. Results related to sensors  $\hat{\mathbf{C}}_2$  and  $\hat{\mathbf{C}}_3$  display intermediate results and are not shown here. The

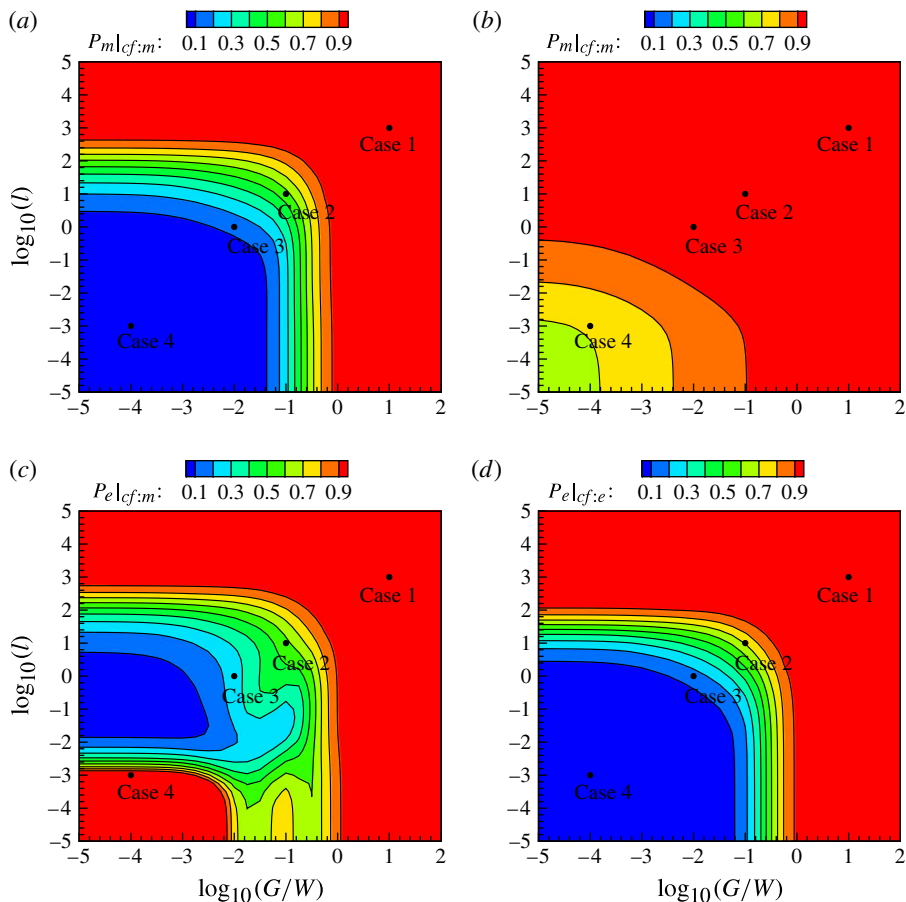


FIGURE 8. Contours of the performance measures  $P_m$  and  $P_e$  as a function of noise-to-signal ratio  $G/W$  and control cost parameter  $l$ : (a)  $P_m|_{cf:m}$  using estimation sensor  $\hat{\mathbf{C}}_1$ ; (b)  $P_m|_{cf:m}$  using  $\hat{\mathbf{C}}_4$ ; (c)  $P_e|_{cf:m}$  using  $\hat{\mathbf{C}}_1$ ; and (d)  $P_e|_{cf:e}$  using  $\hat{\mathbf{C}}_1$ .

measurement-based performance  $P_m$  of the compensator is defined as

$$P_m = \left[ \frac{\int_{-\infty}^{+\infty} |\hat{\mathbf{C}}_p \hat{\mathbf{X}}_\omega|^2 d\omega}{\bar{m}_0^2} \right]^{1/2}, \tag{4.4}$$

where  $\hat{\mathbf{X}}_\omega$  is given by (4.3) and  $\bar{m}_0^2$  is the measurement energy related to the uncontrolled case. Each plot shows iso-contours of  $P_m$  in the  $(G/W, l)$ -plane. Contours with ‘hot’ colours (red) indicate parameter combinations where the control has been ineffective in reducing the measurement energy; contours with ‘cold’ colours (blue) point to values of  $(G/W, l)$  where the perturbation measure has been reduced successfully. The convergence of the performance  $P_m$  towards one (ineffective closed-loop control) is common to all sensor configurations as either the control cost  $l$  or the noise-to-signal ratio  $G/W$  exceeds a critical value. This parameter regime

---

Case	$l$	$G/W$	$P_m _{cf:m}$	$P_e _{cf:m}$	$P_m _{cf:e}$	$P_e _{cf:e}$
1	$10^3$	$10^1$	1.000	1.000	1.000	1.000
2	$10^1$	$10^{-1}$	0.566	0.574	0.784	0.707
3	$10^0$	$10^{-2}$	0.135	0.254	0.292	0.157
4	$10^{-3}$	$10^{-4}$	0.026	1.084	0.037	0.005

---

TABLE 2. Performance measures based on measurement energy (subscript  $m$ ) or global perturbation energy (subscript  $e$ ). The compensator has been designed using a cost functional based on measurement energy (subscript  $cf : m$ ) or on global perturbation energy (subscript  $cf : e$ ). Four selected cases, ranging from the small-gain limit to the large-gain limit, are presented.

---

corresponds to small-gain limit situations where either the control gain  $\hat{K}$  or the Kalman gain  $\hat{L}$  approach zero. For small noise-to-signal ratios  $G/W$  and small control parameters  $l$  (inexpensive control), the estimator provides an accurate approximation of the state, which is subsequently multiplied by a non-zero control gain to obtain a positive action on the perturbation. As a result, the performance measure  $P_m$  is rather small in this parameter regime since both the estimator and the controller reach their large-gain limit and behave at their best. The compensator based on sensor  $\hat{C}_1$  is, by a considerable margin, the most efficient, with a performance parameter  $P_m$  equal to 0.026 in the large-gain limit; this means that only 2.6% of the uncontrolled measurement energy remains after control is applied. As the sensor location for the estimator is moved further downstream, though, the performance parameter  $P_m$  rises substantially in the large-gain region: 17, 36 or 71% of the uncontrolled measurement energy could not be removed by the compensator using sensors  $\hat{C}_2$ ,  $\hat{C}_3$  or  $\hat{C}_4$ , respectively. This exercise clearly demonstrates that an actuator placed near the edge of the step requires a sensor located in its vicinity, if satisfactory performance of the compensator is to be expected. In what follows, we will concentrate on sensor  $\hat{C}_1$  and further probe its performance behaviour and limitations.

More physical insight into the compensated system can be gained by computing the transfer function between the noise  $w$  and the performance measurement  $m_p$ . Four cases, labelled accordingly in figure 8(a), are analysed in detail: case 1 is representative of an ineffective compensator in the small-gain limit, both cases 2 and 3 characterize a system with average performance, while case 4 corresponds to a compensator operating in the large-gain limit. As we shall see later, case 4 has been included to probe the edge of performance robustness and the characteristics of its breakdown beyond this limit. The governing parameters, i.e. the noise-to-signal ratio and control cost, for these cases are summarized in table 2 (second and third columns) together with values of various performance measures.

In figure 9(a) the magnitude of the transfer function from  $w(t)$  to  $m_p(t)$  for each of the four cases is displayed, and results pertaining to the uncontrolled system are overlaid in black symbols. As expected, the compensator operating in the small-gain limit (case 1, shown in red) does not act on the flow and the transfer function is identical to the uncontrolled one. By progressively reducing the noise-to-signal ratio and the control parameter (light blue and dark blue curves), the most amplified frequencies are considerably reduced and the compensator becomes effective over a wider range of frequencies, even though frequencies above  $\omega \approx 1.5$  are slightly more amplified compared to the uncontrolled case. This tendency continues until the

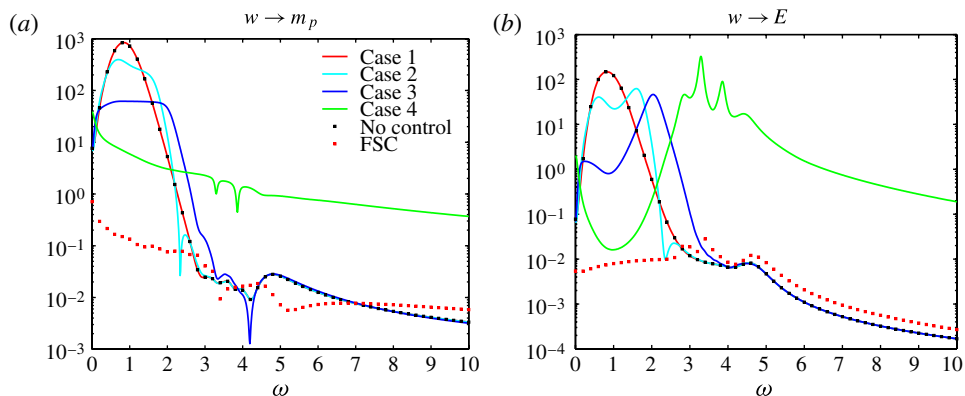


FIGURE 9. (a) Magnitude of the transfer function  $|m_{pw}|$  for four different  $(G/W, l)$  parameter settings, as well as the uncontrolled case. (b) Transfer function between noise and global energy for the same four parameter settings. The full-state control (FSC) transfer function has been obtained for  $l = 10^{-3}$  (large-gain limit).

large-gain limit (in green) is reached: the low frequencies ( $\omega < 2$ ), which would be naturally amplified by the uncontrolled system, have been successfully suppressed, which explains the very good performance of the compensator with  $P_m = 0.026$  (see table 2, fourth column).

The results above confirm the successful manipulation of the inherent amplification behaviour (see figure 2a) of the uncontrolled flow: the pronounced response to low frequencies has been strongly reduced by the compensator.

#### 4.2.2. Response in the frequency domain: effect on the perturbation energy

Even though the controller is designed based on the measurement  $m_p$  only, the performance of the compensator can also be evaluated by the reduction of the perturbation energy in the entire domain. This is possible in the present case since our ROM is based on POD modes, and therefore accurately captures the energy of the original system. This point has particular implications for experimental control set-ups where reduced-order models are typically obtained by identification techniques based on input and output data. By construction, such models cannot express or capture state information, and the question arises whether targeting the measurement energy in the cost functional produces commensurate reductions in the entire perturbation energy. While the control gain is still based on the measurement-based cost functional  $J_m$ , we therefore evaluate the global energy performance measure

$$P_e = \frac{\int_{-\infty}^{+\infty} \|\hat{X}_\omega\|^2 d\omega}{\bar{E}_0}, \quad (4.5)$$

with  $\hat{X}_\omega$  from (4.3) and  $\bar{E}_0$  as the energy based on the uncontrolled system. The ratio  $P_e$  of the perturbation energy for the compensated case to the perturbation energy for the uncontrolled case is depicted in the  $(G/W, l)$ -plane in figure 8(c). This plot shows similar characteristics to figure 8(a) but also displays important differences. For large values of  $G/W$  and  $l$  (the small-gain limit for estimator and controller), the control action is negligible and no reduction in the perturbation energy is achieved ( $P_e = 1$ ).



For moderate estimation and control cost parameters, the performance parameter  $P_e$  decreases, and it appears that a reduction in measurement energy (measured by  $P_m$ ) brings about a proportional reduction in the overall perturbation energy. However, as the large-gain limit is approached (case 4), the value of  $P_e$  increases again, even above one, indicating that the perturbation energy of the controlled case exceeds the energy of the uncontrolled case. The measurement energy, however, is efficiently reduced, as by design.

As before, the transfer function between the noise and the energy in the domain  $\|\hat{X}_\omega\|^2$  provides more details of the observed behaviour (see figure 9b). Case 1 (in red) represents the small-gain limit, and the transfer function coincides with that for the uncontrolled flow since no control action is exerted on the flow. As  $G/W$  and  $l$  are reduced (light blue curve), the dominant, inherently amplified frequencies around  $\omega = 1$  are reduced by the compensator but higher frequencies appear near  $\omega = 1.8$ . Nonetheless, the energy in the entire domain diminishes ( $P_e = 0.458$ ) – see values in table 2 (fifth column). This trend continues as the governing parameters are further decreased (dark blue curve). Finally, in the large-gain limit (green curve), the dominant frequencies of the uncontrolled system ( $\omega \approx 1$ ) have been reduced by four decades, while the energy in higher frequencies ( $\omega > 2$ ) has been amplified by four orders of magnitude. This amplification outweighs the control effort on the lower frequencies, thereby leading to an increase in the overall energy of the system ( $P_e = 1.085$ ) and a failure of the compensator when measured in the global energy norm. The reason for this behaviour may stem from the location of the spatial support of the optimal response at high frequencies. As mentioned in § 2.2, this support is upstream of sensor  $\mathbf{C}_p$  for  $\omega > 2$ . Hence,  $m_p$  cannot capture the naturally amplified perturbations (the optimal response) in this frequency range. This may explain the failure of the compensator to stabilize the energy in high frequencies, since the objective functional of the compensator is precisely the measurement energy based on  $m_p$ .

#### 4.3. Performance of the compensator using a cost functional based on the energy

We conclude by basing the controller design on the cost functional  $J_e$  and by directly targeting the perturbation energy in the entire domain. In figure 8(d), we show in the  $(G/W, l)$ -plane the performance parameter  $P_e$ . We observe that in the large-gain limit (small values of  $G/W$  and  $l$ ), the compensator now efficiently reduces the perturbation energy  $P_e = 0.005$ . From table 2 (column 6), we also note that the perturbation measurement is significantly reduced, i.e.  $P_m = 0.037$ .

## 5. Closed-loop control using linearized Navier–Stokes simulations

In the last section, we have studied the performance of the designed compensator with the reduced-order model  $\text{ROM}_{150}$  as the plant. We will now assess the performance of this compensator in the case of the large-scale LDNS, i.e. the full, unreduced model for flow over a rounded backward-facing step, as the plant. In many flow control studies, this represents the essential performance test of the compensator. As the ROM reproduces all input–output dynamics from the LDNS with an error less than 1%, we expect that the results of the study presented in §§ 3 and 4 remain valid for the case of the compensated LDNS. We will see that this is indeed true for the case of small and medium gains (§§ 5.1 and 5.2) but, for larger gains (§ 5.3), instabilities arise in the compensated system.

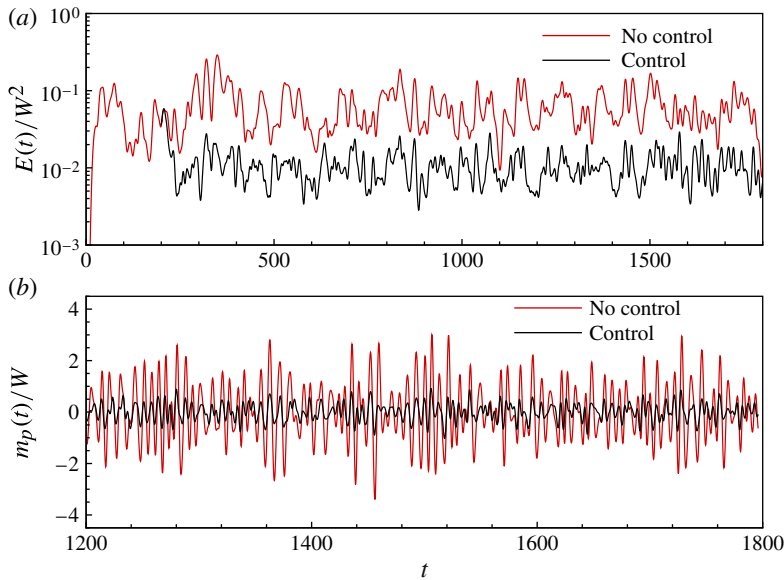


FIGURE 10. (Colour online) Temporal evolution of the energy based on an LDNS continuously forced by random noise. The compensator has been designed under linear assumptions (case 3). (a) Perturbation energy for the uncontrolled (grey/red online) and controlled (black) cases. (b) Measurement energy for the uncontrolled (grey/red online) and controlled (black) cases.

### 5.1. Analysis of case 3 ( $l = 10^0$ and $G/W = 10^{-2}$ )

We first consider the medium-gain case (case 3 with  $l = 10^0$  and  $G/W = 10^{-2}$ ) and use the cost-functional  $J_e$  as our objective for the controller. We choose again the best-performing estimator based on sensor  $\mathbf{C}_1$ , which will be referred to by  $\mathbf{C}$  in what follows. The plant is given by the discretized system of (2.3); a second-order scheme is used for the time integration. A white Gaussian noise is supplied to  $w(t)$ , and a statistically steady state is obtained after some time. The performance measures  $P_m$  and  $P_e$  defined in (4.4) and (4.5) may be evaluated in the simulations by time averaging  $|\mathbf{C}_p \mathbf{X}|^2$  and  $\mathbf{X}^* \mathbf{Q} \mathbf{X}$ , respectively. The results should be comparable to those of the ROM study (§ 4) since the simulation has been given a white Gaussian noise in time, which statistically feeds all frequencies by an equal amount.

Figure 10(a) juxtaposes the temporal evolution of energy for the uncontrolled simulation (in grey/red online) and the evolution of energy for the compensated simulation (in black), where the same excitation sequence  $w(t)$  has been used to ensure a fair comparison. Starting from a zero initial state, a transient phase is observed that quickly evolves into a statistically stationary state. The time for a particle to be convected from the actuator location  $B_2$  to the reattachment point (sensor  $\mathbf{C}_p$ ) is approximately 20 time units. The total simulation time  $T = 1800$  is almost 100 times larger, thus ensuring adequate convergence of the statistical properties of the flow. At  $t = 200$  the compensator is switched on (black curve). The energy rapidly decreases to levels nearly one decade smaller than in the uncontrolled simulation. For completeness, the measurement signal  $m_p(t)$  is displayed in figure 10(b) for the uncontrolled (grey/red online) and compensated (black) simulation. Again, a distinct reduction in variance of the signal can be observed.

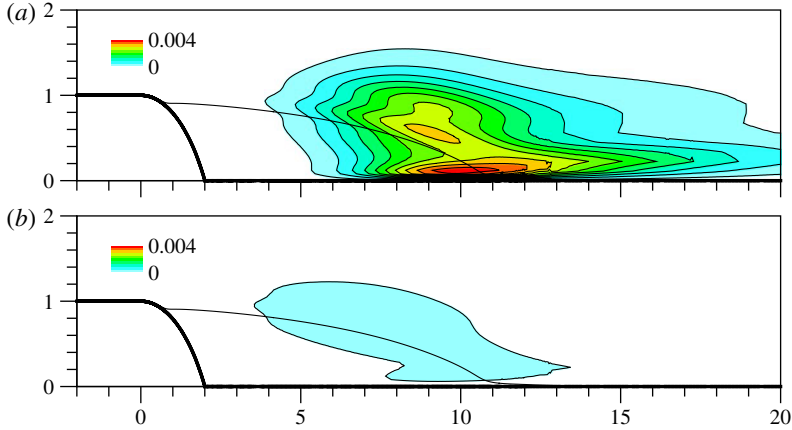


FIGURE 11. Pointwise mean perturbation kinetic energy  $\overline{k'}/W^2$  of simulations with random forcing: (a) uncontrolled LDNS; (b) compensated LDNS (case 3).

	ROM	LDNS ( $W = 1$ )	DNS ( $W = 0.1$ )	DNS ( $W = 1$ )	DNS ( $W = \sqrt{10}$ )
$P_e$	0.157	0.17	0.17	0.41	0.63
$P_m$	0.292	0.30	0.31	0.64	0.84
$\overline{k'_{max}}/U_\infty^2$ (%)		0.42	0.0042	0.31	1.96
$\overline{k'_{max} _c}/U_\infty^2$ (%)		0.07	0.0007	0.12	1.34
$\overline{k'_{max} _c}/\overline{k'_{max}}$		0.16	0.16	0.37	0.69

TABLE 3. Performance evaluation of linear and nonlinear simulations: column 2, based on the ROM (§ 4); column 3, based on LDNS with random noise (§ 5); and columns 4–6, based on DNS with random noise with  $W = 0.1$ ,  $W = 1$  and  $W = \sqrt{10}$  (§ 6).

The third column of table 3 contains the performance measures  $P_e$  and  $P_m$  corresponding to the above simulation. The values are nearly identical to those obtained for the ROM (the numbers from table 2 have been reproduced in the second column). It is evident that the overall perturbation energy  $P_e$  and the perturbation measurement energy  $P_m$  have been reduced by a factor of 0.17 and 0.30, respectively. These results underline the validity of the overall procedure followed within this paper.

Finally, figure 11 displays contours of the pointwise perturbation mean kinetic energy (normalized by the variance of the input noise)  $\overline{k'}/W^2$  for the uncontrolled (figure 11a) and controlled (figure 11b) simulations. The pointwise kinetic energy of the perturbation is taken as  $k'(x, y, t) = (u'^2 + v'^2)/2$ , and the overline designates the time average. The perturbation energy increases along the shear layer due to a convective instability; its maximum is reached near  $x = 10$ . This pointwise mean kinetic energy distribution for the uncontrolled case is closely related to the optimal response given in figure 2(c). The mean kinetic energy contours for the controlled simulation deviate significantly, as the effectiveness of the compensator is clearly demonstrated by the greatly reduced energy levels in the shear-layer region. Table 3 (column 3) shows that the maximum (over space) perturbation mean kinetic energy is

lowered by a factor of  $1/0.16 \approx 6$ . Figure 11 is of interest to experimental studies of flow control, as it provides a direct comparison of local turbulence levels throughout the recirculation bubble for the uncontrolled and controlled case.

### 5.2. Analysis of control cost

We will next assess the characteristics of the control cost. We first note that the penalization term  $u^2$ , appearing in the objective functionals  $J_m$  and  $J_e$  introduced in §4, is not representative of the true energy expended by the user for control. We therefore resort to an analysis of the energy budget: evaluate the user-supplied power to the system associated with  $u(t)$  and compare it to a physical quantity that describes the realized gain by controlling the flow. To this end, we recall the linearized Navier–Stokes equations (2.3) in continuous form,

$$\partial_t \mathbf{v}' + \mathbf{V} \cdot \nabla \mathbf{v}' + \mathbf{v}' \cdot \nabla \mathbf{V} = -\nabla p' + Re^{-1} \nabla^2 \mathbf{v}' + w(t) \mathbf{b}_1 + u(t) \mathbf{b}_2, \quad \nabla \cdot \mathbf{v}' = 0, \quad (5.1)$$

where  $\mathbf{v}'$  is the perturbation velocity and  $\mathbf{V}$  the base flow. Taking the inner product of this equation with  $\mathbf{v}'$ , averaging over time and integrating in space over a domain  $\Omega$  (which includes the spatial support of  $b_2$ , but excludes that of  $b_1$ ) yields

$$\begin{aligned} & \int_{\partial\Omega} (\overline{k' \mathbf{V} \cdot \mathbf{n}} + \overline{p' \mathbf{v}' \cdot \mathbf{n}} - 2Re^{-1} \overline{\mathcal{D}' \cdot \mathbf{v}' \cdot \mathbf{n}}) ds \\ &= \iint_{\Omega} (\overline{u(t) \mathbf{b}_2 \cdot \mathbf{v}'} - \overline{\mathcal{R}' : \mathcal{D}} - 2Re^{-1} \overline{\mathcal{D}' : \mathcal{D}'}) d\Omega \end{aligned} \quad (5.2)$$

where  $:$  denotes the contraction operator or Frobenius inner product, defined as  $\mathbf{A} : \mathbf{B} = \sum_{ij} A_{ij} B_{ij} = \text{trace}(\mathbf{A}^* \mathbf{B})$ . This equation governs the flux of the mean kinetic perturbation energy  $\overline{k'}$  across the boundary  $\partial\Omega$ , given by  $\int_{\partial\Omega} \overline{k' \mathbf{V} \cdot \mathbf{n}} ds$ . It is written in conservative form, and various volume source terms appear on the right-hand side of the equation that contribute to this flux. The mean external power  $\overline{u(t) \mathbf{b}_2 \cdot \mathbf{v}'}$  represents the mean power supplied by the user during the control effort. The production term  $-\overline{\mathcal{R}' : \mathcal{D}}$  involves the Reynolds stress tensor  $\mathcal{R}'$  and the strain-rate tensor  $\mathcal{D}$  of the base flow. In the case of an amplifier flow, this term will supply the main power (drawn from the base flow  $\mathbf{V}$ ), which in turn will trigger high values of the mean fluctuating kinetic energy flux. Even though this term may be positive or negative, in the case of an amplifier flow it should be predominantly and strongly positive. The dissipation term  $2Re^{-1} \overline{\mathcal{D}' : \mathcal{D}'}$  contains the strain-rate tensor  $\mathcal{D}'$  of the perturbations and accounts for the mean power lost due to viscous stresses. Lastly, not only the power supplied to the system enters the mean fluctuating kinetic energy flux, there are two other terms: the mean velocity–pressure correlation  $\int_{\partial\Omega} \overline{p' \mathbf{v}' \cdot \mathbf{n}} ds$  and the viscous diffusion term  $\int_{\partial\Omega} -2Re^{-1} \overline{\mathcal{D}' \cdot \mathbf{v}' \cdot \mathbf{n}} ds$ .

We have evaluated the various integrals appearing in (5.2) for the case described in §5.1. For  $\Omega$  we chose the domain  $-0.1 \leq x \leq 11.3$ . The left boundary at  $x = -0.1$  is downstream of  $\mathbf{b}_1$ , but upstream of  $\mathbf{b}_2$ , such that the domain  $\Omega$  comprises the actuator  $\mathbf{b}_2$  and extends downstream beyond the reattachment point. The line integrals along the wall and in the far field yield zero contributions, and we are thus left only with contributions from the line integrals at  $x = -0.1$  and  $x = 11.3$ . In table 4, the numerical values of the non-zero line integrals at  $x = -0.1$  and  $x = 11.3$  as well as the various source terms in  $-0.1 \leq x \leq 11.3$  are listed for the uncontrolled and controlled simulations. For the uncontrolled case, we identify the kinetic energy flux at the boundaries as the dominant term among the line integrals, with a pronounced increase between the inlet ( $x = -0.1$ ) and the outlet ( $x = 11.3$ ). This feature is linked

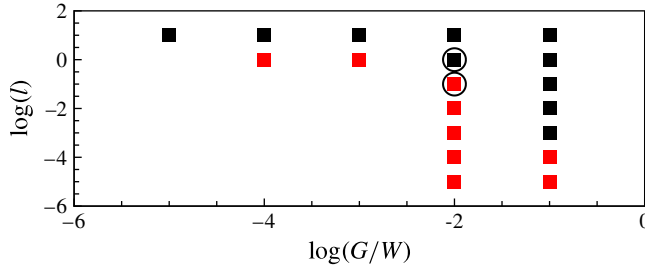


FIGURE 12. (Colour online) Instabilities in the compensated linearized numerical simulation. The grey (red online) squares (respectively, black squares) represent unstable (respectively, stable) results. The circles refer to the ‘medium-gain’ and ‘large-gain’ cases studied in depth in § 5.3.2.

Control	At $x = -0.1$			At $x = 11.3$			Sources in $-0.1 \leq x \leq 11.3$		
	$\bar{k}V$	$\overline{p'v'}$	Visc.	$\bar{k}V$	$\overline{p'v'}$	Visc.	Power	Prod.	Dissip.
Off	-0.0058	-0.00082	-0.000025	1.5	0.69	0.0017	0	3.8	-1.7
On	-0.0058	-0.00079	-0.000025	0.16	0.068	0.0023	0.004	0.56	-0.34

TABLE 4. Evaluation of the control cost in the linearized simulations. All values are to be multiplied by  $10^{-3}$ . The compensator has been designed for  $l = 10^0$  and  $G/W = 10^{-2}$  (case 3).

to the convective Kelvin–Helmholtz instability, which gives rise to strong disturbance growth along the shear layer of the separation bubble. Closer inspection of the source terms shows that this growth in kinetic energy flux is mainly due to the production term, which is more than twice the dissipation term in magnitude (while the power term is zero due to the absent control input). The production term is the ‘engine’ of the instability, located along the shear layer of the separation bubble. Clearly, any effective control effort should target this term in order to reduce the amount of unsteadiness in the flow. For the controlled simulation, similar features can be observed; yet the increase in kinetic energy flux between the boundaries of the domain  $\Omega$  is significantly smaller (by a factor of 10, as shown in column 5 of table 4). The source terms (columns 8–10) show that the production and dissipation terms have decreased accordingly, while the user-supplied power term from the control effort remains negligible in the process. For a minute cost of control (for our case, a value of 0.004) we have attained a substantial reduction of kinetic energy flux between the uncontrolled and controlled simulation (in our case,  $1.50 - 0.16 = 1.34$ ) – indeed a highly efficient effort. Of course, this efficiency is due to the fact that we control an instability, i.e. the strong convective instability as the source of unsteadiness is taken advantage of to actively suppress it.

### 5.3. Behaviour of compensated systems for larger gains – robustness and sensitivity

This section is devoted to a performance evaluation of the compensator for the case of larger gains. Simulations with the randomly forced, linearized Navier–Stokes equations for a range of control costs  $l$  and noise-to-signal ratios  $G/W$  have shown that strong instabilities can arise in the compensated system. Figure 12 reports stable

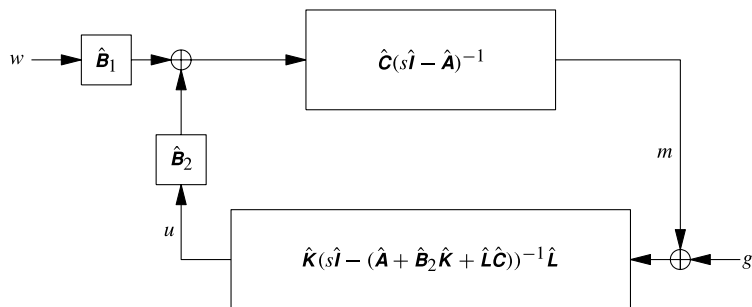


FIGURE 13. Block diagram for the robustness and internal stability analysis, showing the plant and compensator transfer function as well as relevant input and output signals.

(black symbols) and unstable (grey symbols, red online) parameter combinations. For sufficiently large  $l$  or  $G/W$  (black symbols), the response behaviour of the linearized simulation is close to the response of model ROM<sub>150</sub> (as observed in the medium-gain case in § 5.1). The linearized DNS then reaches the same performance measures as the ones displayed in figure 8(d). Cases 1–3, studied in §§ 3 and 4, belong to this category as well, with equivalent performances of the linearized DNS. On the other hand, we also encountered cases in which the linearized DNS exhibited instabilities as a compensator was applied (indicated by grey symbols (red online) in figure 12). These cases concentrate at the large-gain limit in the  $(G/W, l)$ -plane; case 4, studied in §§ 3 and 4, falls into this category. This instability phenomenon should not come as a surprise, since it is well known from the control literature (see Doyle 1978) that, although stability bounds for the LQR problem can be stated, the same is not true for the LQG problem. In the latter cases, a case-by-case sensitivity analysis will detect and quantify the presence of an instability in the compensated system.

A discrepancy between the model of the plant on which a compensator is based and the model of the plant the compensator is intended to ultimately control can cause a decline in compensator performance or, in more severe cases, an instability in the compensated system. In what follows, we will address robustness and sensitivity issues due to uncertainties in the model.

It is worth mentioning that for our case a robustness study is necessary and relevant, since the estimation sensor has been placed downstream of the control location, and, consequently, the influence of the control  $u$  on the measurement  $m$  may render the feedback loop unstable. An analysis of the stability margins of the compensated system, as presented below, is thus sensible. The work of Bagheri *et al.* (2009) also treats convectively unstable flows (boundary layers), but, in contrast, the estimation sensor is invariably located upstream of the controller. This configuration is thus in pure feed-forward mode, and the compensated systems are never unstable. For this reason, the issue of robustness for boundary layer studies did not have to be raised.

Robustness analysis for compensated systems is closely linked to the concept of internal stability. It is based on the feedback loop consisting of the plant and the compensator, which is externally driven by either measurement noise  $g$  or the external noise environment  $w$  (see figure 13). Two transfer functions, describing the dynamics between  $w$  and measurement  $m$  and the dynamics between  $g$  and  $m$ , have to be analysed as to their amplification characteristics. Physically, the external noise environment  $w$  is an essential component of any amplifier flow since it drives its



$$\begin{aligned}
 w \rightarrow m \quad m &= \frac{\hat{\mathbf{C}}(s\hat{\mathbf{I}} - \hat{\mathbf{A}})^{-1} \hat{\mathbf{B}}_1}{1 - \hat{\mathbf{T}}_P \hat{\mathbf{T}}_K} w \\
 g \rightarrow m \quad m &= \frac{\hat{\mathbf{T}}_P \hat{\mathbf{T}}_K}{1 - \hat{\mathbf{T}}_P \hat{\mathbf{T}}_K} g
 \end{aligned}$$

TABLE 5. Transfer functions between noise sources  $g$  and  $w$  and the measurement  $m$  for the compensated system.

dynamics. Consequently, it provides a pervasive and bounded excitation. Internal stability then ensures that all internal signals of the feedback loop remain bounded as well. In our case, we will concentrate on the measurement  $m$  as the internal signal. The measurement noise  $g$  may also act as a source of excitation, and the dynamics between  $g$  and  $m$  also has to be probed. The transfer functions for either noise to measurement dynamics are given in table 5. They have a common denominator given by  $1 - \hat{\mathbf{T}}_P \hat{\mathbf{T}}_K$ , where

$$\hat{\mathbf{T}}_P(s) \equiv \hat{\mathbf{C}}(s\hat{\mathbf{I}} - \hat{\mathbf{A}})^{-1} \hat{\mathbf{B}}_2, \quad (5.3a)$$

$$\hat{\mathbf{T}}_K(s) \equiv \hat{\mathbf{K}}(s\hat{\mathbf{I}} - (\hat{\mathbf{A}} + \hat{\mathbf{B}}_2 \hat{\mathbf{K}} + \hat{\mathbf{L}} \hat{\mathbf{C}}))^{-1} \hat{\mathbf{L}} \quad (5.3b)$$

are the transfer functions for the plant (subscript  $P$ ) and for the compensator (subscript  $K$ ). It can be shown that the numerators of both transfer functions (i) do not contain unstable poles, as in the case  $w \rightarrow m$ , or (ii) may contain unstable poles that are cancelled by the denominator, as in the case  $g \rightarrow m$ . As a result, zeros of the denominator in the right half-plane can be the only cause of instabilities. We will thus investigate internal stability by tracking the zeros of  $1 - \hat{\mathbf{T}}_P \hat{\mathbf{T}}_K$  in the unstable half-plane. Internal stability is given for LQG compensators in the absence of modelling uncertainties in the plant. However, under practical circumstances, this is rarely true, and robustness analysis is required to quantify the internal stability margins by modifying the plant transfer function while keeping the compensator transfer function constant (i.e. based on the nominal plant transfer function).

Two approaches will be taken. Both assess the internal stability of the feedback loop with respect to modifications of the plant transfer function. In the first, standard approach, these perturbations consist of frequency-independent amplitude and phase modifications of the plant transfer function, while in the second case, an optimization will be performed to determine the worst-case perturbations to the plant transfer function.

### 5.3.1. Presentation of a standard robustness analysis

To probe the stability margins, two type of perturbations are applied: a change in the magnitude of the transfer function, and a change in the phase of the transfer function. Mathematically, we have

$$\hat{\mathbf{T}}_P \rightarrow a \hat{\mathbf{T}}_P, \quad (5.4a)$$

$$\hat{\mathbf{T}}_P \rightarrow e^{i\phi} \hat{\mathbf{T}}_P. \quad (5.4b)$$

The first modification represents an error in the growth rates of the convective instabilities; the second modification represents an error in the travel time of perturbations between the actuator and the sensor.

We define the minimum gain margin  $GM^+$  as the minimum value of the amplitude  $a$ , greater than one, that achieves marginal stability in the transfer functions  $w \rightarrow m$  or  $g \rightarrow m$ . For this we seek  $a$  which ensures that  $1 - a\hat{\mathbf{T}}_P\hat{\mathbf{T}}_K$  has one zero with zero real part while all other zeros are located in the left half-plane. The maximum gain margin  $GM^-$  is defined analogously: it corresponds to the maximum value of amplitude  $a$ , less than one, that achieves marginal stability. Lastly, the phase margin  $PM$  is the minimum positive value of  $\phi$  such that  $1 - e^{i\phi}\hat{\mathbf{T}}_P\hat{\mathbf{T}}_K$  exhibits a marginal zero (i.e. with zero real part). More formally, if we define a function of the amplitude  $a$  as  $f(a) = \max_k \text{Re}\{s_k(a) \mid 1 - a\hat{\mathbf{T}}_P(s)\hat{\mathbf{T}}_K(s) = 0\}$ , the minimum gain margin  $GM^+$  is the smallest zero of  $f$  greater than one, while the maximum gain margin  $GM^-$  is the largest zero of  $f$  less than one. If we define a function of the phase angle  $\phi$  as  $g(\phi) = \max_k \text{Re}\{s_k(\phi) \mid 1 - e^{i\phi}\hat{\mathbf{T}}_P(s)\hat{\mathbf{T}}_K(s) = 0\}$ , the phase margin  $PM$  is the smallest positive zero of  $g$ .

The robustness analysis described above has been applied to our compensated system, and results are given in figure 14, which displays iso-contours of the various internal stability margins as a function of control cost  $l$  and noise-to-signal ratio  $G/W$ . The coloured contours are overlaid by black contours showing the performance measure  $P_e$ . In addition, symbols have been added to the  $(G/W, l)$ -plane to indicate stable (black circles) or unstable (white circles) compensated simulations. In the limit of small gains and low noise-to-signal ratio, we observe significant internal stability margins and thus good robustness, with gain margins of more than 6 dB for the amplitude and  $60^\circ$  for the phase angle. In contrast, for large gains the stability margins are substantially reduced, in both gain and phase margin. Case 3, which results in an efficient compensated DNS, is characterized by internal stability margins of  $GM^+ = 1.91$  dB,  $GM^- = -9.41$  dB and  $PM = 14.1^\circ$ . For only slightly larger gains,  $GM^+$ ,  $1/GM^-$  and  $PM$  drop off rather precipitously since case 3 is located in a parameter regime distinguished by large gradients for  $GM^+$ ,  $GM^-$  and  $PM$ . For case 4, we obtain  $GM^+ = 0.047$  dB,  $GM^- = -0.138$  dB and  $PM = 0.68^\circ$ , which amounts to exceedingly small stability margins. This explains the observed (in)stability of the compensated DNS.

### 5.3.2. Presentation of a worst-case sensitivity analysis

A technique that is more common in fluid dynamics aims at determining the worst-case scenario for internal instability. For this analysis, we consider general perturbations to all components of the plant transfer function and write

$$\hat{\mathbf{T}}_P \rightarrow \mathbf{T}_P = \mathbf{C}(s\mathbf{I} - \mathbf{A})^{-1}\mathbf{B}_2, \tag{5.5}$$

where  $\mathbf{A}$ ,  $\mathbf{B}_2$  and  $\mathbf{C}$  deviate from the nominal system matrices  $\hat{\mathbf{A}}$ ,  $\hat{\mathbf{B}}_2$  and  $\hat{\mathbf{C}}$ . The stability condition based on the zeros of  $1 - \mathbf{T}_P\mathbf{T}_K$  translates into finding the unstable eigenvalues of the matrix

$$\mathbf{M} = \begin{pmatrix} \mathbf{A} & \mathbf{B}_2\hat{\mathbf{K}} \\ -\hat{\mathbf{L}}\mathbf{C} & \hat{\mathbf{A}} + \hat{\mathbf{B}}_2 + \hat{\mathbf{L}}\hat{\mathbf{C}} \end{pmatrix}. \tag{5.6}$$

We look for  $\mathbf{A}$ ,  $\mathbf{B}_2$  and  $\mathbf{C}$  that lead to marginal stability of the matrix  $\mathbf{M}$ , with a given eigenvalue displaying a zero amplification rate. To constrain the optimization, we introduce an error measure that describes the disparity between the transfer function of

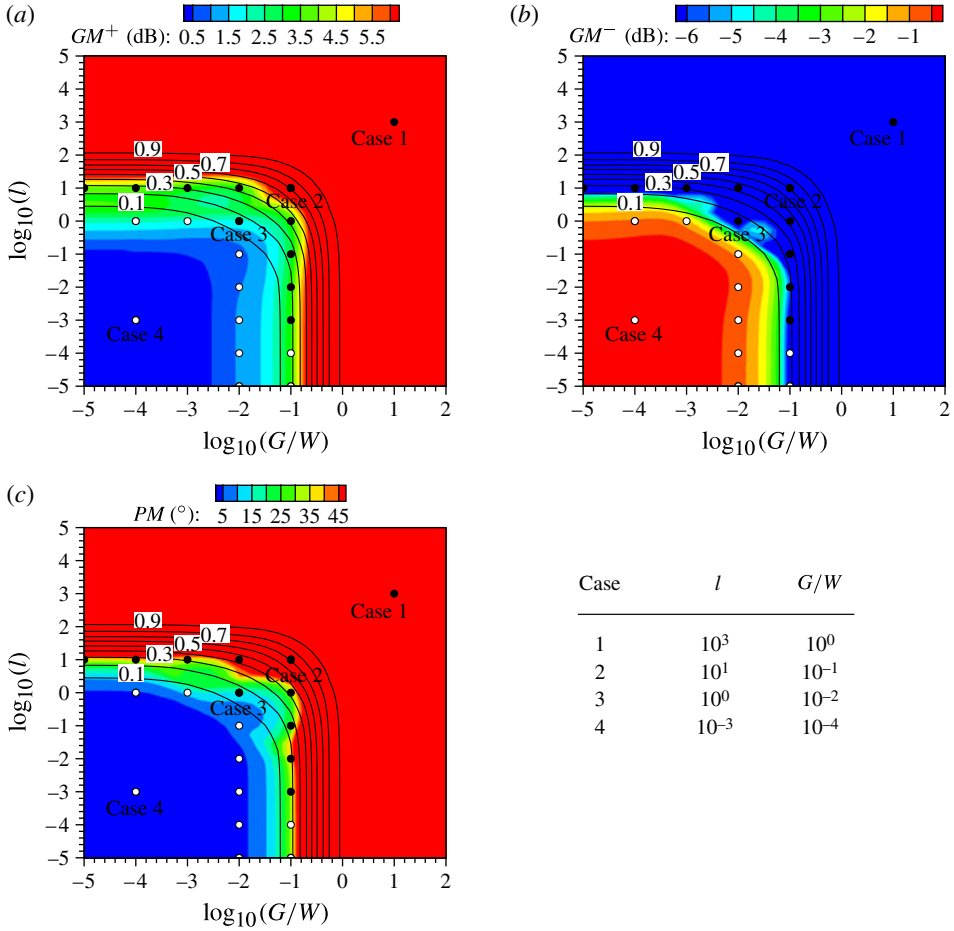


FIGURE 14. (a) Iso-contours of gain margin as a function of noise-to-signal ratio  $G/W$  and control cost  $l$ . (b) Same as (a) for the downside gain margin. (c) Same as (a) for the phase margin. Superimposed on the plots (in black) are contours of the performance measure  $P_e$ . Furthermore, the black symbols indicate stable compensated numerical simulations, while white symbols mark unstable compensated simulations.

the original plant model and of the nominal plant. We have

$$err(\mathbf{A}, \mathbf{B}_2, \mathbf{C}) = \left[ \frac{\int_{-\infty}^{i\infty} |\mathbf{T}_P - \hat{\mathbf{T}}_P|^2 ds}{\int_{-\infty}^{i\infty} |\hat{\mathbf{T}}_P|^2 ds} \right]^{1/2}, \quad (5.7)$$

with  $\hat{\mathbf{T}}_P = \hat{\mathbf{C}}(s\hat{\mathbf{I}} - \hat{\mathbf{A}})^{-1} \hat{\mathbf{B}}_2$  and  $\mathbf{T}_P = \mathbf{C}(s\mathbf{I} - \mathbf{A})^{-1} \mathbf{B}_2$ . We will then determine the minimal distance to instability of  $\mathbf{M}$  by adjusting the components  $\mathbf{A}$ ,  $\mathbf{B}_2$  and  $\mathbf{C}$  of the plant model (taken as matrices of size  $150 \times 150$ ,  $150 \times 1$  and  $1 \times 150$ , respectively) while maintaining a given error  $err$  between the respective transfer functions. Details of the optimization procedure are given in appendix B.

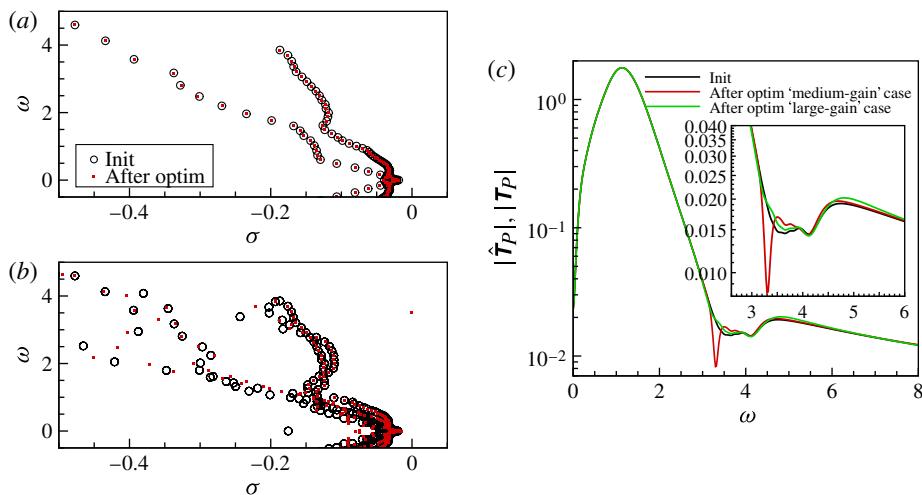


FIGURE 15. (Colour online) Example from the sensitivity analysis. (a,b) Spectra of plant  $\mathbf{A}$  and compensated system  $\mathbf{M}$  for the medium-gain case. The circles indicate the plant based on  $(\hat{\mathbf{A}}, \hat{\mathbf{B}}_2, \hat{\mathbf{C}})$  while the grey (red online) squares indicate the plant governed by the optimal  $(\mathbf{A}, \mathbf{B}_2, \mathbf{C})$  found by the optimization algorithm. (c) Modulus of the transfer functions  $\hat{T}_P$  and  $T_P$  for the medium-gain case ( $l = 10^0$ ,  $G/W = 10^{-2}$ ,  $err = 0.00375$ ,  $\omega_{opt} = 3.3$ ) and the large-gain case ( $l = 10^{-1}$ ,  $G/W = 10^{-2}$ ,  $err = 0.00125$ ,  $\omega_{opt} = 3.3$ ).

Figure 15 shows a typical example from our sensitivity analysis where the compensated system becomes unstable for a particularly small error  $err$  of the transfer function. For the medium-gain case, the optimization process, performed for  $\omega_{opt} = 3.3$  and  $err = 0.00375$ , yields a nearly unmodified spectrum for  $\mathbf{A}$  (figure 15a) but strong modifications of the compensated spectrum for  $\mathbf{M}$  (figure 15b). In both panels, the circles represent the spectrum of the plant based on  $(\hat{\mathbf{A}}, \hat{\mathbf{B}}_2, \hat{\mathbf{C}})$  while the grey squares (red online) pertain to a plant governed by the optimal  $(\mathbf{A}, \mathbf{B}_2, \mathbf{C})$  determined by the optimization algorithm. The compensated system clearly displays a marginal eigenvalue at the optimization frequency  $\omega_{opt} = 3.3$  (see figure 15b), which is in accordance with the high value of  $\lambda_\omega = 7.5 \times 10^4$  found for the singular value of  $\mathbf{R}^{-1}$ . Further insight can be gained from a comparison of the transfer functions  $\hat{T}_P$  and  $T_P$ ; the modulus of the respective transfer functions is depicted in figure 15(c). It is evident that the response behaviour  $u \rightarrow m$  for the optimized plant (dark grey line, red online) exhibits a small error near the optimization frequency  $\omega_{opt} = 3.3$ . For comparison, the transfer function modulus for the large-gain case, obtained for  $\omega_{opt} = 3.3$  and  $err = 0.00125$ , is also displayed (in grey, green online). The large-gain transfer function is even closer to the original transfer function (black curve) but, nonetheless, displays a very high value for the largest singular value of  $\mathbf{R}^{-1}$ , namely,  $\lambda_\omega = 2 \times 10^4$ . This latter finding corroborates, for the large-gain case, the high sensitivity of the compensated system to minute variations in the transfer function  $u \rightarrow m$  in the frequency band  $\omega \approx 2.6$ –6. The sensitivity is less pronounced for the medium-gain case.

It may appear that, in certain parameter ranges, the LQG design is particularly sensitive to modelling errors; one should keep in mind, however, that the above sensitivity analysis is based on worst-case scenarios, and that under realistic conditions the observed sensitivity may be less severe.

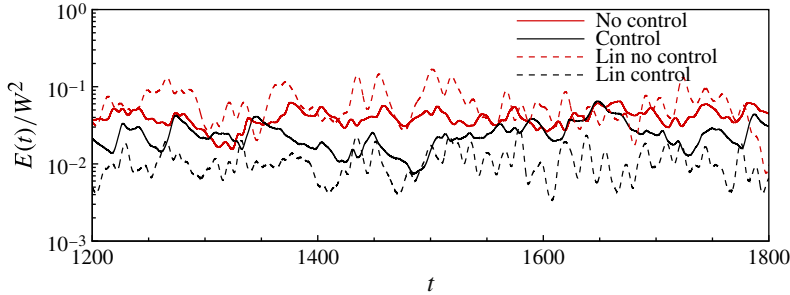


FIGURE 16. (Colour online) Temporal evolution of the mean perturbation energy based on a DNS continuously forced by finite-amplitude noise  $W = \sqrt{10}$ . The compensator has been designed under linear assumptions (case 3). The linear case has been added in dashed lines and scaled to the initial energy of the nonlinear simulations.

## 6. Nonlinear effects

The controller has been designed for perturbations governed by linear dynamics. With nonlinear governing equations, this situation is recovered if the amplitude of the perturbations is and remains very small over the entire domain, which may be achieved using very small amplitude for the upstream noise, i.e.  $W \ll 1$ . In the previous section, we have seen that small-amplitude noise may be suppressed by a controller designed under the assumption of a linear governing equation. In the present section, we will gradually increase the amplitude  $W$  of the incoming perturbations; nonlinear effects will progressively be introduced and their impact on the overall performance of the linear compensator under off-design conditions can be studied. A similar test has been conducted by Ilak (2009) for impulsive initial conditions.

We have tested three different amplitudes:  $W = 0.1$  (see the supplementary movie available at [journals.cambridge.org/flm](http://journals.cambridge.org/flm)),  $W = 1$  and  $W = \sqrt{10}$ . The performance measures  $P_e$  and  $P_m$  corresponding to the three cases are reported in table 3 (columns 4–6). The simulations have been run up to  $t = 1800$ , as in the linear simulation of § 5. The random noise sequence from the linear case has been used, which allows a direct comparison with the linear results (reported in column 3). In table 3, the maximum pointwise mean kinetic energy of the uncontrolled and controlled (indicated by  $|\cdot|_c$ ) simulations are listed together with their ratio. For a small noise amplitude  $W = 0.1$ , the evolution of the uncontrolled perturbation is quasi-linear, and the performance of the compensator is nearly the same as in the linear case (compare columns 3 and 4 of table 3). The performance measures  $P_e$  and  $P_m$ , however, gradually deteriorate as the noise amplitude  $W$  increases (compare columns 4–6 of table 3).

In figure 16, the temporal evolution of the mean perturbation energy is displayed for the large-amplitude case  $W = \sqrt{10}$ ; the uncontrolled simulation is shown in grey (red online), the compensated one in black. The oscillations of the energy curves for the nonlinear case (solid curve) are less pronounced than in the linear case (dashed line). The same observation can be made for the compensated simulation. It is seen that the mean energy level of the perturbation is reduced by the linear compensator, but a noticeable loss in performance is apparent.

As before, the pointwise perturbation mean kinetic energy  $\bar{k}'/W^2$  gives further insight into the temporal evolution of the energy as the disturbances advect along the shear layer. In figure 17(a,b) the pointwise perturbation mean kinetic energy from the

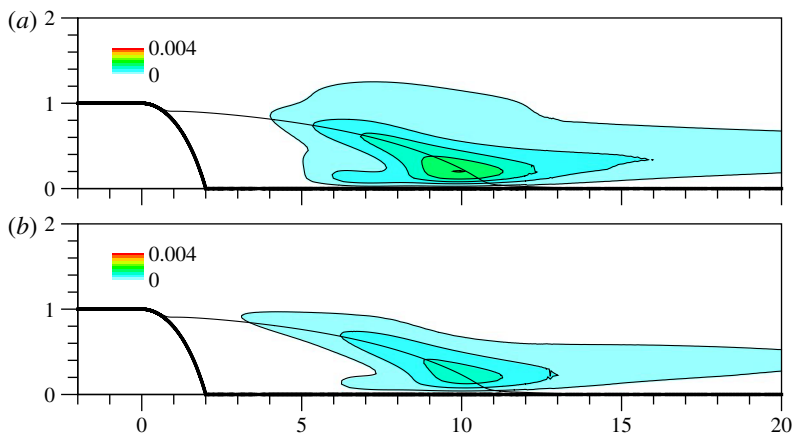


FIGURE 17. Pointwise perturbation mean kinetic energy  $\bar{k}'/W^2$  of simulations with random forcing for  $W = \sqrt{10}$ : (a) uncontrolled DNS; and (b) compensated DNS (case 3).

nonlinear simulation with random noise is displayed for the case with  $W = \sqrt{10}$ . The colour map has been adjusted to permit direct comparison with the equivalent linear results given in figure 11; significant differences from the linear case can be observed. Figure 17(a), illustrating the uncontrolled case, displays saturation effects caused by nonlinearities; the overall shape of the maximum energy contours are, however, similar to the linear case – concentrating on the dynamics in the shear layer and the reattachment area. For the compensated case (figure 17b), the energy is maximal in the shear layer but is, again, lower than in the uncontrolled case; in contrast, the energy is higher than in the linear case for  $x > 10$ , indicating the appearance of nonlinear structures, which are more difficult to control. We notice that the energy could be less attenuated by control efforts than in the linear case: in table 3 (column 6), a maximum perturbation mean kinetic energy of 1.96% is observed in the uncontrolled simulation, which reduces to 1.34% as the compensator is switched on. The perturbation mean kinetic energy is thus diminished by a modest factor of  $1/0.69 \approx 1.5$  (compared to a factor of  $1/0.17 \approx 6$  for the small-amplitude simulation with  $W = 0.1$ , see column 4). As stronger nonlinearities set in, the linear-based compensator becomes ever less effective.

## 7. Summary and conclusions

Two-dimensional incompressible flow over a rounded backward-facing step, a canonical configuration showing noise-amplifying behaviour, has been controlled by feedback control strategies. Specifically, the LQG framework has been employed in conjunction with POD-based reduced-order models for the plant. Similar techniques have previously been studied (see Ilak & Rowley 2008; Bagheri & Henningson 2011), but with the main emphasis on model reduction aspects. Important issues related to the practical implementation of feedback control laws for amplifier flows have been left unaddressed, which motivated this present investigation.

The analysis of the feedback control set-up first concentrated on the estimation process. A placement of sensors throughout the convectively unstable region of the flow revealed a distinct advantage of measurement input from the most upstream sensor. It further showed that the speed of estimation is more important than the



accuracy of the estimation, while keeping in mind that upstream sensor measurements are more easily corrupted by noise since the signal has not yet been amplified and filtered by the flow. Low-quality sensors should be placed further downstream where the amplitude of the detected signal prevails over the added inherent measurement noise; the resulting delay in estimation, however, will ultimately cause a loss in compensator performance. The noise-to-signal ratio of the sensor thus plays an important role and has been linked to the estimation parameter for the computation of the Kalman gain.

Continuing with the best (most upstream) sensor, the performance of the compensated system has been studied under the idealistic assumptions that the ROM accurately mimics the plant. The noise-to-signal ratio (or estimation parameter)  $G/W$  and the cost-of-control parameter  $l$  have been varied to cover a range of control scenarios from the small-gain limit (SGL), where the compensator is ineffective, to the large-gain limit (LGL), where the compensator operates at its maximal performance. An excess total energy can be observed when the measurement energy is taken as the control objective; this phenomenon may be linked to the inability of the sensor  $C_p$  to detect optimal responses with high frequency ( $\omega > 2$ ). However, this shortcoming can be overcome by basing the cost functional for the controller design on the total energy  $J_e$ .

A compensator designed with  $J_e$  has then been applied to the full, linearized Navier–Stokes equations driven by continuous stochastic forcing. In the case of medium gains, the compensated system reacted as predicted by the ROM-based model study, and a substantial reduction in perturbation energy could be accomplished. A detailed, term-by-term analysis of contributions to the energy budget showed that the control action was extremely efficient: a very weak user-supplied actuation power generated a substantial (order one) gain in the kinetic energy flux near the reattachment location. For compensators designed with larger gains, instabilities in the compensated linearized Navier–Stokes equations arose: even if the compensator is stable for the model it was designed for, its stability can no longer be implied or assured when applied to a slightly different plant. This loss of stability has been analysed using two approaches, one based on classical Nyquist analysis, the other on a worst-case analysis, which is more common to fluid dynamical applications. Both analyses showed a reduction in internal stability margins as the large-gain limit is approached. This established that the POD model was particularly sensitive to high frequencies (around  $\omega \approx 3$ –6). Hence, for a compensator to work efficiently with large gains (in order to achieve maximal performance), the ROM (based upon which the compensator was designed) is required to be very precise also at low energies and high frequencies.

Nonlinear effects have been reintroduced to the closed-loop control problem by applying the compensator, designed under linear assumptions, to the nonlinear Navier–Stokes equations and attempting to suppress continuous noise sources of progressively higher amplitude  $W$ . Minor deviations have been detected for small-amplitude noise; in the large-amplitude case, however, the compensator performance deteriorated owing to the appearance of nonlinearly triggered structures.

It can be concluded from our study that designing closed-loop control strategies for amplifier flows is significantly more involved than the equivalent design for oscillator flows. While in this latter case instabilities are generally narrow-band in frequency and thus more easily detectable/controllable, a noise amplifier produces more broadband signals and magnifies physical and non-physical perturbations alike. For this latter reason, a comprehensive study of the sensitivity of the compensator

	$\mathbf{C}_1$	$\mathbf{C}_2$	$\mathbf{C}_3$	$\mathbf{C}_4$	$\mathbf{C}_p$	$E$
$\mathbf{B}_1$	0.99	0.60	0.62	0.66	0.74	0.77
$\mathbf{B}_2$	0.61	0.34	0.33	0.32	0.30	0.28

TABLE 6. The relative  $\mathcal{H}_2$ -errors (in %) for the various input–output combinations. The error on the energy has been evaluated using the following expression:  $\{\int_{-\infty}^{+\infty} [(\hat{X}_\omega^* \hat{X}_\omega)^{1/2} - (X_\omega^* \mathbf{Q} X_\omega)^{1/2}]^2 d\omega / \int_{-\infty}^{+\infty} X_\omega^* \mathbf{Q} X_\omega d\omega\}^{1/2}$ .

performance with respect to various noise sources is imperative for a successful closed-loop control design. Transfer functions, i.e. frequency-based input–output relations, are particularly helpful in pinpointing strong sensitivities, in placing sensors efficiently, and in avoiding undesirable parameter regimes. It is hoped that the present study has introduced and demonstrated effective tools that – despite the inherent challenges – aid in the design of effective closed-loop control strategies for amplifier flows.

Supplementary movies are available at [journals.cambridge.org/flm](http://journals.cambridge.org/flm).

### Appendix A. Reduced-order model

In view of our control objectives, the ROM should be able to capture accurately the dynamic response of the output variables ( $\mathbf{C}_{1,2,3,4,p}$  given by sensors and the perturbation energy  $E(t)$ ) to forcings by the two input variables ( $\mathbf{B}_{1,2}$ ). We choose a model reduction technique based on standard POD, which transforms flow-state snapshots, arising from harmonic forcings introduced via the terms  $\mathbf{B}_1$  and  $\mathbf{B}_2$ , into a finite-dimensional orthogonal basis onto which the full flow equations are projected. An analysis of the ROM confirmed a satisfactory balance between accuracy and size. Details of this type of analysis are given in Dergham *et al.* (2011) for the same backward-facing step configuration using a single input  $\mathbf{B}_2$ .

In our case, a ROM based on a Galerkin projection of the full system onto the first 150 POD modes has been selected owing to its good performance and comparatively small size. The transfer functions of the full system have been computed by Fourier-transforming signals from the impulse responses of the linearized DNS. The errors between the transfer functions of the reduced-order models and the linearized DNS have been measured using the  $\mathcal{H}_2$ -norm. Table 6 presents these errors for different combinations of input triggering and output sensing. We note that the impulse responses triggered by  $\mathbf{B}_2$  are more accurately captured than those triggered by  $\mathbf{B}_1$ . All errors are below 1%.

### Appendix B. Sensitivity analysis

The worst-case sensitivity analysis outlined in § 5.3.2 proceeds in the following manner. We first note that a marginal eigenvalue  $s = i\omega$  of the matrix  $\mathbf{M}$  is equivalent to the largest singular value  $\lambda_\omega$  of the resolvent matrix tending to infinity. The resolvent matrix corresponds to the matrix  $\mathbf{R}^{-1}$  with  $\mathbf{R} = i\omega\mathbf{I} - \mathbf{M}$ . Formulating an optimization problem, we will try to maximize, for a given frequency  $\omega$ , the functional  $\lambda_\omega^2(\mathbf{A}, \mathbf{B}_2, \mathbf{C})$  as a function of  $\mathbf{A}$ ,  $\mathbf{B}_2$  and  $\mathbf{C}$ . The optimum will be sought under the constraint that the transfer function error  $err(\mathbf{A}, \mathbf{B}_2, \mathbf{C})$  maintains a prescribed error  $\epsilon$ . The constrained optimization problem is transformed into an unconstrained problem

via a penalization technique, and a Polak–Ribière conjugate-gradient method coupled to a line-search algorithm is used to determine the optimum.

More specifically, we denote by  $\lambda_\omega$  the largest singular value of  $\mathbf{R}^{-1}$  where  $\mathbf{R} = i\omega\mathbf{I} - \mathbf{M}$  and  $\mathbf{M}$  is the matrix defined in (5.6). We furthermore introduce  $(\mathbf{F}, \mathbf{G})^\top$  and  $(\mathbf{X}, \mathbf{Y})^\top$  as the principal right and left singular vectors associated with  $\lambda_\omega$ , which satisfy

$$\mathbf{R}^{-1*} \mathbf{R}^{-1} \begin{pmatrix} \mathbf{F} \\ \mathbf{G} \end{pmatrix} = \lambda_\omega^2 \begin{pmatrix} \mathbf{F} \\ \mathbf{G} \end{pmatrix}, \quad \begin{pmatrix} \mathbf{X} \\ \mathbf{Y} \end{pmatrix} = \mathbf{R}^{-1} \begin{pmatrix} \mathbf{F} \\ \mathbf{G} \end{pmatrix}. \quad (\text{B } 1)$$

The sensitivity analysis is formulated as an optimization problem for determining the minimal stability margin for a specified discrepancy between two transfer functions. We begin with the following Lagrangian:

$$L = \lambda_\omega^2 - \begin{pmatrix} \tilde{\mathbf{Y}} \\ \tilde{\mathbf{X}} \end{pmatrix}^* \left[ \mathbf{R} \begin{pmatrix} \mathbf{X} \\ \mathbf{Y} \end{pmatrix} - \begin{pmatrix} \mathbf{F} \\ \mathbf{G} \end{pmatrix} \right] - \begin{pmatrix} \tilde{\mathbf{F}} \\ \tilde{\mathbf{G}} \end{pmatrix}^* \left[ \lambda_\omega^2 \mathbf{R}^* \begin{pmatrix} \mathbf{F} \\ \mathbf{G} \end{pmatrix} - \begin{pmatrix} \mathbf{X} \\ \mathbf{Y} \end{pmatrix} \right]. \quad (\text{B } 2)$$

Rendering this Lagrangian stationary with respect to the variables  $(\mathbf{F}, \mathbf{G})^\top$ ,  $(\mathbf{X}, \mathbf{Y})^\top$  and  $\lambda_\omega^2$  yields the following expressions for the Lagrange multipliers (denoted by an over-tilde):

$$\begin{pmatrix} \tilde{\mathbf{F}} \\ \tilde{\mathbf{G}} \end{pmatrix} = \mathbf{R}^{-1} \begin{pmatrix} \mathbf{F} \\ \mathbf{G} \end{pmatrix}, \quad \begin{pmatrix} \tilde{\mathbf{Y}} \\ \tilde{\mathbf{X}} \end{pmatrix} = \lambda_\omega^2 \begin{pmatrix} \mathbf{F} \\ \mathbf{G} \end{pmatrix}, \quad \begin{pmatrix} \mathbf{F} \\ \mathbf{G} \end{pmatrix}^* \begin{pmatrix} \mathbf{F} \\ \mathbf{G} \end{pmatrix} = 1. \quad (\text{B } 3)$$

Setting the first variation of the Lagrangian with respect to the control variable  $\mathbf{R}$  to zero results in an expression for the variation of the squared singular value given by

$$\delta\lambda_\omega^2 = -2\lambda_\omega^2 \operatorname{Re} \left[ \begin{pmatrix} \mathbf{F} \\ \mathbf{G} \end{pmatrix}^* \delta \mathbf{R} \begin{pmatrix} \mathbf{X} \\ \mathbf{Y} \end{pmatrix} \right]. \quad (\text{B } 4)$$

Using (5.6), this expression for  $\delta\lambda_\omega^2$  may be expressed in terms of variations in the matrices  $\mathbf{A}$ ,  $\mathbf{B}_2$  and  $\mathbf{C}$ . We obtain

$$\delta\lambda_\omega^2 = 2\lambda_\omega^2 \operatorname{Re}(\mathbf{F}\mathbf{X}^*) : \delta\mathbf{A} + 2\lambda_\omega^2 \operatorname{Re}(\mathbf{F}\mathbf{Y}^* \hat{\mathbf{K}}^*) : \delta\mathbf{B} - 2\lambda_\omega^2 \operatorname{Re}(\mathbf{X}\mathbf{G}^* \hat{\mathbf{L}}) : \delta\mathbf{C}^*, \quad (\text{B } 5)$$

where  $:$  denotes the contraction operator or Frobenius inner product, defined as  $\mathbf{A} : \mathbf{B} = \sum_{ij} A_{ij} B_{ij} = \operatorname{trace}(\mathbf{A}^* \mathbf{B})$ .

The constraint of a user-prescribed error  $\gamma$  (measured in the  $\mathcal{H}_2$ -norm) between the full and reduced transfer function may be approximated in the following manner:

$$\mu_\gamma(\mathbf{A}, \mathbf{B}_2, \mathbf{C}) = -\gamma^2 + \sum_j \underbrace{|\mathbf{C}(i\omega_j\mathbf{I} - \mathbf{A})^{-1} \mathbf{B} - \hat{\mathbf{C}}(i\omega_j\mathbf{I} - \hat{\mathbf{A}})^{-1} \hat{\mathbf{B}}|^2}_{\phi_j} \Delta\omega_j. \quad (\text{B } 6)$$

In the above expression  $\Delta\omega_j$  are quadrature coefficients. In our case, we chose a simple first-order approximation of the integral with  $\Delta\omega_j = 0.02$  and integration

limits  $\omega_{min} = -10$ ,  $\omega_{max} = 10$ . The first variation of this functional reads

$$\begin{aligned} \delta\mu_\gamma &= \left( 2 \sum_j \operatorname{Re} [\phi_j (-i\omega_j \mathbf{I} - \mathbf{A}^*)^{-1} \mathbf{C}^* \mathbf{B}^* (-i\omega_j \mathbf{I} - \mathbf{A}^*)^{-1}] \Delta\omega_j \right) : \delta\mathbf{A} \\ &+ \left( 2 \sum_j \operatorname{Re} [\phi_j (-i\omega_j \mathbf{I} - \mathbf{A}^*)^{-1} \mathbf{C}^*] \Delta\omega_j \right) : \delta\mathbf{B} \\ &+ \left( 2 \sum_j \operatorname{Re} [\phi_j^* (i\omega_j \mathbf{I} - \mathbf{A})^{-1} \mathbf{B}] \Delta\omega_j \right) : \delta\mathbf{C}^*. \end{aligned} \quad (\text{B } 7)$$

Lastly, we combine the above expressions and consider the unconstrained minimization problem

$$J_{\omega,\gamma}(\mathbf{A}, \mathbf{B}_2, \mathbf{C}) = -\arctan(\ln(\lambda_\omega^2)/\alpha) + \beta\mu_\gamma^2 + \arctan(\ln(v_\omega^2)/\alpha), \quad (\text{B } 8)$$

with  $\beta$  as the penalty coefficient. In our computations, we used  $\alpha = 10$  and  $10^3 \leq \beta \leq 10^{10}$ . Note that the third term in (B 8) penalizes the largest singular value  $v_\omega$  of  $\mathbf{S}^{-1}$  where  $\mathbf{S} = i\omega \mathbf{I} - \mathbf{A}$ . This is simply to avoid convergence of the optimization algorithm towards solutions where  $s = i\omega$  is an eigenvalue of  $\mathbf{A}$ , which is an undesirable solution. With  $\mathbf{H}$  and  $\mathbf{Z}$  as the principal right and left singular vectors of  $\mathbf{S}$  corresponding to  $v_\omega$  and satisfying  $\mathbf{S}^* \mathbf{S} \mathbf{H} = v_\omega^2 \mathbf{H}$  and  $\mathbf{Z} = \mathbf{S} \mathbf{H}$  with  $\mathbf{H}^* \mathbf{H} = 1$ , we can express the first variation of  $v_\omega^2$  in the form  $\delta v_\omega^2 = 2v_\omega^2 \operatorname{Re}(\mathbf{H} \mathbf{Z}^*) : \delta\mathbf{A}$ .

#### REFERENCES

- AHUJA, S. & ROWLEY, C. W. 2010 Feedback control of unstable steady states of flow past a flat plate using reduced-order estimators. *J. Fluid Mech.* **645**, 447–478.
- ÅKERVIK, E., HEPFFNER, J., EHRENSTEIN, U. & HENNINGSON, D. S. 2007 Optimal growth, model reduction and control in a separated boundary-layer flow using global modes. *J. Fluid Mech.* **579**, 305–314.
- ALIZARD, F., CHERUBINI, S. & ROBINET, J.-C. 2009 Sensitivity and optimal forcing response in separated boundary layer flows. *Phys. Fluids* **21**, 064108.
- ARCHAMBAUD, J. P., ARNAL, D., HEIN, S., MELO DE SOUZA, J., HANIFI, A., GODDARD, J. L., KRIER, J. & DONELLI, R. 2008 Use of laminar flow technologies for supersonic drag reduction – results of FP project SUPERTRAC. In *Proceedings of the 5th European Congress on Computational Methods in Applied Sciences and Engineering (ECCOMAS), Venice, Italy*.
- BAGHERI, S., BRANDT, L. & HENNINGSON, D. S. 2009 Input–output analysis, model reduction and control of the flat-plate boundary layer. *J. Fluid Mech.* **620**, 263–298.
- BAGHERI, S. & HENNINGSON, D. S. 2011 Transition delay using control theory. *Phil. Trans. R. Soc. A* **369**, 1365–1381.
- BARBAGALLO, A., SIPP, D. & SCHMID, P. J. 2009 Closed-loop control of an open cavity flow using reduced-order models. *J. Fluid Mech.* **641**, 1–50.
- BEWLEY, T. R. & LIU, S. 1998 Optimal and robust control and estimation of linear paths to transition. *J. Fluid Mech.* **365**, 305–349.
- BLACKBURN, H. M., BARKLEY, D. & SHERWIN, S. J. 2008 Convective instability and transient growth in flow over a backward-facing step. *J. Fluid Mech.* **603**, 271–304.
- BOIKO, A. V., DOVGAL, A. V. & HEIN, S. 2008 Control of a laminar separating boundary layer by induced stationary perturbations. *Eur. J. Mech. (B/Fluids)* **27** (4), 466–476.
- BURL, J. B. 1999 *Linear Optimal Control.  $\mathcal{H}_E$  and  $\mathcal{H}_\infty$  Methods*. Addison-Wesley.
- CHEVALIER, M., HEPFFNER, J., ÅKERVIK, E. & HENNINGSON, D. S. 2007 Linear feedback control and estimation applied to instabilities in spatially developing boundary layers. *J. Fluid Mech.* **588**, 163–187.

- DERGHAM, G., SIPP, D., ROBINET, J.-C. & BARBAGALLO, A. 2011 Model reduction for fluids using frequential snapshots. *Phys. Fluids* **23**, 064101.
- DOYLE, J. 1978 Guaranteed margins for LQG regulators. *IEEE Trans. Autom. Control* **23** (4), 756–757.
- EHRENSTEIN, U., PASSAGGIA, P.-Y. & GALLAIRE, F. 2011 Control of a separated boundary layer: reduced-order modeling using global modes revisited. *Theor. Comput. Fluid Dyn.* **25** (1–4), 195–207.
- GHARIB, M. & ROSHKO, A. 1987 The effect of flow oscillations on cavity drag. *J. Fluid Mech.* **177**, 501–530.
- HECHT, F., PIRONNEAU, O., HYARIC, A. LE & OHTSUKA, K. 2005 Freefem++, 3rd edition, version 3.19, <http://www.freefem.org/ff++>, Université Pierre et Marie Curie Paris, Laboratoire Jacques-Louis Lions.
- ILAK, M. 2009 Model reduction and feedback control of transitional channel flow. PhD thesis, Princeton University, Mechanical and Aerospace Engineering.
- ILAK, M. & ROWLEY, C. W. 2008 Modeling of transitional channel flow using balanced proper orthogonal decomposition. *Phys. Fluids* **20**, 034103.
- JOSHI, S. S., SPEYER, J. L. & KIM, J. 1997 A systems theory approach to the feedback stabilization of infinitesimal and finite-amplitude disturbances in plane Poiseuille flow. *J. Fluid Mech.* **332**, 157–184.
- JOSLIN, R. D. 1998 Overview of laminar flow control. NASA Rep. TP 208705.
- KIM, J. 2003 Control of turbulent boundary layers. *Phys. Fluids* **15**, 1093–1105.
- KIM, J. & BEWLEY, T. R. 2007 A linear systems approach to flow control. *Annu. Rev. Fluid Mech.* **39**, 383–417.
- MARQUET, O., SIPP, D., CHOMAZ, J.-M. & JACQUIN, L. 2008 Amplifier and resonator dynamics of a low-Reynolds number recirculation bubble in a global framework. *J. Fluid Mech.* **605**, 429–443.
- ROSSITER, J. E. 1964 Wind tunnel experiments on the flow over rectangular cavities at subsonic and transonic speeds. *Aero. Res. Council. R&M* 3438.
- ROWLEY, C. W. 2005 Model reduction for fluids using balanced proper orthogonal decomposition. *Intl J. Bifurcation Chaos* **15**, 997–1013.
- SARIC, W. S., REED, H. L. & WHITE, E. B. 2003 Stability and transition of three-dimensional boundary layers. *Annu. Rev. Fluid Mech.* **35**, 413–440.
- SIPP, D., MARQUET, O., MELIGA, P. & BARBAGALLO, A. 2010 Dynamics and control of global instabilities in open flows: a linearized approach. *Appl. Mech. Rev.* **63**, 030801.
- SIROVICH, L. 1987 Turbulence and the dynamics of coherent structures. *Q. Appl. Maths* **45**, 561–590.